Multi-catalytic active sites biochar-based catalysts for glucose isomerize to fructose: experiments and density functional theory study

Xiheng Kang [1], Zi You [1], Yongheng Huang [1], Jian Peng [1], Junhua Zhang [2], Arthur J. Ragauskas [3, 4, 5], Zhanying Zhang [6, 7], Xueping Song [1*]

[1] Guangxi Key Laboratory of Clean Pulp & Papermaking and Pollution Control, College of Light Industry and Food Engineering, Guangxi University, Nanning 530004, PR China

[2] Jiangsu Co-Innovation Center of Efficient Processing and Utilization of Forest Resources, College of Chemical Engineering, Nanjing Forestry University, Nanjing 210037, China

[3] Department of Chemical and Biomolecular Engineering, University of Tennessee, Knoxville, TN, USA

[4] Joint Institute for Biological Sciences, Biosciences Division, Oak Ridge National Laboratory, Oak Ridge, TN, USA

[5] Center for Renewable Carbon, Department of Forestry, Wildlife and Fisheries, The University of Tennessee, Knoxville, TN 37996, USA

[6] School of Mechanical Faculty of Engineering Medical and Process Engineering, Queensland University of Technology, Brisbane, Queensland 4000, Australia

[7] Center for Agriculture and the Bioeconomy Faculty of Science, Queensland University of Technology, Brisbane, Queensland 4000, Australia

*Corresponding author

Xueping Song

Abstract

Highly efficient prepare fructose is essential for valorizing cellulose to value-added chemicals. This work provides an innovative method for preparing different isomerization catalysts by impregnating different proportions of $MgCl_2$ and $AlCl_3$ and combining different K compounds on cellulose-derived biochar, followed by hydrothermal carbonization and further pyrolysis. Results show active sites of MgO and $Al(OH)_3$ existing in $_4$Mg-$_1$Al-C catalyst can obtain better catalytic effect on glucose isomerization than the singe of Al species presenting in $_0$Mg-$_1$Al-C catalyst. Moreover, the synergism effects of the multi-catalytic active sites such as β-, γ-$Al(OH)_3$, KCl, MgO, and $K_4H_2(CO_3)_3$ in Mg-Al-$KHCO_3$-C catalyst can further lead to an increase in catalytic efficiency of glucose isomerization, compared to the $_4$Mg-$_1$Al-C catalyst. The X-Ray diffraction results present that the value of O/Al in Mg-Al-$KHCO_3$-C catalyst is as high as 13.38, which provides many oxygen vacancies and unsaturated acidic catalysis sites and benefits the glucose isomerization. Simultaneously, the TPD results reveal that the main active sites (MgO, $Al(OH)_3$, and $K_4H_2(CO_3)_3$) in Mg-Al-$KHCO_3$-C catalyst can provide weakly acidic, basic sites, and avoid strongly acidic and basic sites to excess attack the glucose. Based on the density functional theory and wave function analysis, the results indicate that the MgO has a great effect on the ring-opening reaction to form acyclic glucose, while $Al(OH)^{3+}$ has a great effect on promoting acyclic glucose hydrogen transfer isomerize to form fructose. Compared to other carbon-based metal catalysts, the Mg-Al-C-$KHCO_3$-C prepared has excellent catalytic performance, which gives a higher fructose yield (38.7%) and selectivity (87.72%), and catalyzes excellent glucose conversion (44.12%) at 100 ºC in 30 min. In this study, we develop a highly efficient Mg-Al-K-biochar catalyst for glucose isomerization and provide an efficient method for cellulose valorization.

Keywords: biochar; catalyst; isomerization; fructose; cellulose

1 Introduction

The rational utilization of biomass for the production of chemicals is a challenge of global interest owing to the gradual depletion of fossil feedstocks. As a main part of lignocellulosic biomass, cellulose is a polymer composed of several glucose monomers linked through β-1,4-glycosidic bonds, which can be used to extensively produce glucose via hydrolysis [1-4]. However, the high chemical stability of glucose hampers its transformation to other chemicals. Therefore, many researches have proposed high value utilization strategies of cellulose regard not glucose but fructose as a substrate for the synthesis of fuels and chemicals [5-10]. Fructose, structurally similar to glucose, is chemically more active than glucose and is easily converted to different molecules such as 5-hydroxymethylfurfural (5-HMF), furfural, and levulinic acid (LA). Currently, enzymatic glucose isomerization is a main method to produce fructose. However, glucose isomerase has some disadvantages, including low stability, poor accessibility, and harsh reaction conditions [11-13]. In addition to the enzyme, the highest yield of fructose (55%) reported to date is obtained using zeolites as catalysts and it is a two-step synthesis procedure with methanol and water as solvents [7]. However, organic solvents as reaction solvents will somehow cause environmental pollution and increase the cost of fructose separation and purification. To achieve a more environmentally friendly catalytic system, aqueous as reaction solvents and solid Brønsted basic and Lewis acidic catalysts are currently the most suggested catalysts for glucose isomerization.

Biochar is a solid product with a carbon skeleton and is rich in oxygen-containing functional groups [14-16]. It has a large specific surface area and a tunable pore structure, thus has been widely used in high-quality solid carbon-based carriers of catalysts [17-23]. Compared to inorganic materials-based carriers (zeolite), the weak interaction forces between the carbon-based carriers and the active sites make the carbon-base carriers unable to achieve high stability. The low cost controlled physical and chemical properties make them comparable to inorganic materials-based carriers catalysts in terms of catalytic efficiency. The catalytic efficiency of carbon-based catalysts usually can be enhanced by modifying the physical properties such as porosity, specific surface area, and crystalline structure of biochar [24]. Presently, researchers have shown that the catalytic efficiency of carbon-based catalyst for glucose isomerization enhanced by the chemical loading of metal-active sites is higher than that of catalysts by optimizing the physical properties of biochar. Lewis acidic catalysts have been studied in great detail, both experimentally and theoretically [20, 25]. Acidic catalysts can catalyze glucose to produce fructose in relatively high yields due to the intramolecular proton transfer, but their low efficacy in aqueous media have hampered the application of this technology [26]. In contrast, Brønsted basic catalyst has received less attention because early studies reported its poor selectivity to fructose and low yield of below 10%[27, 28]. The low efficacy reason of Brønsted basic catalysts is due to the formation of an unstable enediol intermediate via intramolecular hydride shift. In the Brønsted base catalysis process, it is difficult to ensure the high glucose conversion and good fructose selectivity by enediol intermediate and further control the selectivity of the enediol intermediate to by-products (e.g. 5-HMF, FA). However, the hydrogen transfer caused by Lewis acid catalyst can efficiently reduce the selectivity of by-products. Therefore, it is necessary to design a solid catalyst combining with the advantages of Lewis acid and

Brønsted base active sites in order to efficiently achieve isomerization catalytic of glucose in an aqueous system.

In this study, a series of Mg-Al-K-C biochar-based catalysts were prepared to provide much different unsaturated catalytic sites (e.g. Lewis acid, Brønsted base) while increasing the species of the active sites to obtain a high efficient isomerization of glucose. Meanwhile, the catalyst's suitability in an aqueous media, including catalyst carriers, glucose conversion, and the selectivity and yield of fructose, are evaluated. The active catalytic sites ($MgCl_2$, $AlCl_3$, $KHCO_3$) and their ratio, their catalytic efficiency, and the mechanisms for glucose isomerization are further defined. This work will provide excellent technical support for developing biochar-based glucose isomerization catalysts and high-quality biomass platform products.

2 Experimental section

2.1 Materials

The cellulose (particle size <50 μm), glucose, fructose, $AlCl_3$, $MgCl_2$, KCl, KOH, $KHCO_3$, and K_2CO_3 used in this work were analytical grade and were purchased from Aladding Co., Ltd. (Shanghai, China). All standard reagents (glucose, fructose) were supplied by Sigma-Aldrich of Merck KGaA Co., Ltd. (Germany) and were used without further purification. Milli-Q® ultrapure water purification system supplied ultrapure water (Merck KGaA, Germany).

2.2 Preparation of biochar

Cellulose (10 grams) and deionized water (100 ml) were mixed in an autoclave reactor (BS-500, Shanghai LABE Instrument Co., Ltd) under room temperature[15]. Then, it was heated to 220 °C and kept for 240 min. After the time was reached, the reactor was cooled rapidly in ice water to stop the reaction. The solid and liquid phase products were separated and collected after centrifugation at 10,000

rpm for 8 min. The obtained solid phase product was washed repeatedly with ethanol and deionized water until the pH of the washed liquid was 7.0. The biochar was eventually obtained after drying to a constant weight at 80 °C, and it is named as C.

2.3 Synthesis of Mg-Al-biochar catalyst

Mg-Al-supported biochar catalysts were prepared by an impregnation method. $MgCl_2$ and $AlCl_3$ were mixed with the ratio of 0:1, 1:1, 2:1, 3:1, 4:1, and 5:1, and the total mass of $MgCl_2$ and $AlCl_3$ accounted for 10 wt.% of C. Then, the mixture ($MgCl_2$, $AlCl_3$, C) was eventually stirred for 4 h and dried at 80 °C to constant weight. The dried mixture was pyrolyzed in a tube furnace under N2 atmosphere (the flow rate was 1.5 L/min) at a ramp rate of 10 °C/min from room temperature to 650 °C and then kept for 60 min at 650 °C. Finally, the Mg-Al-supported biochar catalysts with the Mg/Al ratio of 0:1, 1:1, 2:1, 3:1, 4:1, 5:1 were obtained and are denoted as $_0$Mg-$_1$Al-C, $_1$Mg-$_1$Al-C, $_2$Mg-$_1$Al-C, $_3$Mg-$_1$Al-C, $_4$Mg-$_1$Al-C, $_5$Mg-$_1$Al-C, respectively.

2.4 Synthesis of Mg-Al-K-biochar catalyst

One gram of KCl, KOH, $KHCO_3$, and K_2CO_3 were respectively dissolved in deionized water (60 mL) with the co-impregnated mixture of $MgCl_2$, $AlCl_3$, and C to form a new mixture, and the total mass of KCl, KOH, $KHCO_3$, and K_2CO_3 accounts for 10 wt.% in the new mixture, respectively. Among which, in the Mg-Al co-impregnated mixture, the ratio of $MgCl_2$ and $AlCl_3$ is 4:1, and the total mass of $MgCl_2$ and $AlCl_3$ accounts for 10 wt.% of C. The new mixture was eventually stirred for 4 h and then dried at 80 °C for 12 h to constant weight. The oven-dried mixture was pyrolyzed in a tube furnace, and the conditions were consistent with 2.3. After pyrolyzing, the Mg-Al-K-supported biochar catalysts were obtained, and they are denoted as Mg-Al-KCl-C, Mg-Al-KOH-C, Mg-Al-$KHCO_3$-C, and Mg-Al-K_2CO_3-C corresponding to KCl, KOH, $KHCO_3$, and K_2CO_3, respectively.

2.5 Catalytic experiment

Glucose was dissolved in water to obtain 10 wt./v% glucose aqueous solution, and then the Mg-Al-C catalyst (0.1 g) or Mg-Al-K-C catalyst (0.1 g) was added into the aqueous glucose solution. In the catalytic experiment, the mixture was added in an autoclave reactor (500 mL), and then it was heated to 100 °C and kept for 30 min. During the reaction, the mixture was magnetically stirred at 300 r/min to maintain homogeneity. In order to further clarify the stability of the catalyst, the catalytic efficiency experiments of recovered $_4$Mg-$_1$Al-C and Mg-Al-$KHCO_3$-C catalyst were also carried out. The recovered catalyst was washed with deionized (DI) water to remove the residual monosaccharides and solvents. Then recovered $_4$Mg-$_1$Al-C and Mg-Al-$KHCO_3$-C were respectively dried at 80 °C to constant weight, and the above catalytic experiments were repeated. The number of times of the catalyst used was denoted as X. For example, $_4$Mg-$_1$Al-C-3 means that $_4$Mg-$_1$Al-C catalyst was used three times. All experimental values represent the average of triplicate analyses, where the average standard deviation was 1.5%. The total experiments process are shown in scheme 1.

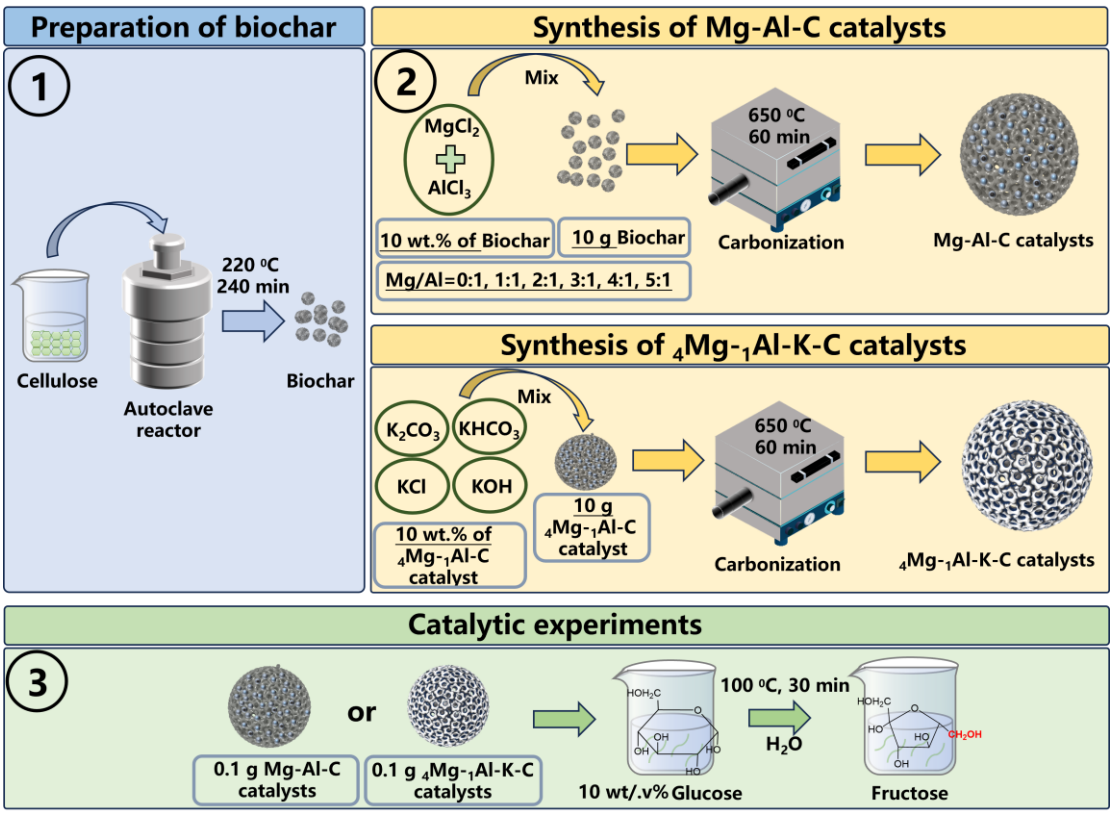

Scheme 1 Experiment process include: **1.** preparation of biochar; **2.** synthesis of Mg-Al-biochar catalysts and $_4$Mg-$_1$Al-K-biochar catalysts; **3**. catalytic experiments.

2.6 Characterization of biochar

Brunauer Emmett Teller [29] surface areas and pore volumes were determined by nitrogen adsorption–desorption isotherm measurements at -196 °C using a gas sorption analyser (Micro Meritics; ASAP 2460). The samples were degassed at 80 °C for 16 h before analysis. The surface morphology and elemental composition of samples were evaluated using scanning electron microscopy (SEM) coupled with energy dispersive X-ray spectroscopy (SEM-EDS; TESCAN MIRA4). The crystalline and amorphous phases were revealed by X-ray direction analysis (XRD; MiniFlex 600) in scanning range of 10–90° at rate of 5°/min at 40 kV and 40 mA [30]. The chemical state of elements on samples surfaces were analyzed using X-ray photoelectron spectroscopy (XPS; Thermo Fisher Scientific K-Alpha ESCA). The metal quantitative analysis of the samples was obtained by an inductively coupled plasma optical emission spectrometer (ICP-OES 700; Agilent Technology). The CO_2-Temperature Programmed

Desorption (CO_2-TPD) and NH_4-Temperature Programmed Desorption (NH_3-TPD) experiments were carried out on a multifunction chemisorption analyzer (AutoChem 1 II 2920, Micro Meritics, USA) and detected by a TCD (Thermal Conductivity Detector). The sample (50 mg) was heated under ultra-high purity He (99.99%) flow (30 mL/min) up to 300 °C at 10 °C/min for 1 h and then it was cooled to 50 °C. After then, CO_2 or NH_3 flow (30 mL/min) passed through the catalyst for 60 min, subsequently, the sample was flushed by He flow (30 mL/min) for 60 min. Then, the TPD analysis was performed under He flow (30 mL/min) by heating the sample at a rate of 15 °C/min up to 650 °C.

2.7 Characterization of catalytic efficiency

The concentrations of glucose and fructose in the liquid phase were quantified by HPLC (Agilent 1200 Series, Santa Clara, CA, USA) using Bio-Rad HPX-87H column (300 × 7.8 mm). Sulfuric acid (5 mM, 0.6 mL/min flow rate) was used as the eluent, and the temperature of the column was maintained at 50 °C. The glucose and fructose concentrations were determined through calibration curves obtained with the reference samples. The conversion of glucose as well as the yield, and selectivity of fructose was calculated follow:

$$C_{Glu}(\%)=\frac{(I_{Glu}-R_{glu})}{I_{Glu}}\times 100\% \quad (1)$$

$$S_{Fru}(\%)=\frac{I_{Glu}}{(I_{Glu}-R_{glu})}\times 100\% \quad (2)$$

$$Y_{Fru}(\%)=\frac{I_{Fru}}{I_{Glu}}\times 100\% \quad (3)$$

where, I_{Glu} and R_{glu} represent the initial and final moles of glucose, respectively. I_{Fru} represents the initial moles of fructose.

2.8 DFT study

All kinetics data were carried out with the Gaussian 16 software [31] and calculated using the M06-2X function [32], in combination with the TZVP basis set [33]. The solvation of water was referenced to

the SMD solvation model [34]. Among them, in order to obtain accurate kinetic data, the Kohn-Sham-DFT single electron Schrödinger equation is used for calculation, as follows:

$$\left(-\frac{\hbar^2}{2m}\triangle^2+V_{eff}(r)\right)\psi_i(r)=\varepsilon_i\psi_i(r) \quad (4)$$

where, $\psi_i(r)$ represents the Kohn-Sham wave function, and εi represents the corresponding energy level. The effective potential field Veff(r) in the equation includes the external potential field and the exchange-correlation potential. Its form is as follows:

$$V_{eff}(r)=V_{ext}(r)+\int\frac{\rho(r')}{|r-r'|}dr'+V_{xc}(r) \quad (5)$$

Where, V_{ext} represents the external potential field, ρ represents the electron density, and V_{xc} represents the exchange-correlation potential.

3 Results and discussion

3.1 Characterization of Mg-Al-biochar catalyst

The actual loadings capacity of Mg^{2+} and Al^{3+} ions in Mg-Al-C catalyst was analyzed by ICP-OES, as shown in **Fig. 1e**. The results show that different load amounts of Mg^{2+} and Al^{3+} ions were successfully loaded onto the biochar. The actual loading ratios of Mg^{2+} and Al^{3+} ions change from 5.37:5.80 to 9.32:2.01, as similar as the theoretical Mg/Al loading ratios. The SEM images and particle distribution size of Mg-Al-C with different Mg/Al loading ratios are shown in **Fig. 1a-d**. From **Fig.1a**, it can be found that the particle size of the $_1$Mg-$_1$Al-C catalyst is mainly distributed between 50-100 nm. From **Fig. 1b**, it can be found that with the Mg content increases, the particle size of the $_2$Mg-$_1$Al-C catalyst is mainly between 100 - 200 nm, higher than those of $_1$Mg-$_1$Al-C catalyst. When the Mg/Al ratio increases to 3:1 and 4:1 **(Fig. 1c, d)**, it can be found that there is a small amount distribution of catalyst particle size at 500 - 600 nm. The results show that the particle size of biochar on the catalyst surface increases gradually with the increase of Mg/Al loading ratios. This may be due to the increase of Mg^{2+} in the Mg/Al loading

ratio, resulting in the formation of much crystalline materials on the surface of biochar sphere. The formation of crystalline will be stick the catalysts with each other. The N_2 adsorption and desorption curves and pore-size distribution of Mg-Al-C catalysts with different Mg/Al loading ratios are shown in **Fig. 1**. According to the International Union of Pure and Applied Chemistry (IUPAC) classification of adsorption curves, all the adsorption and desorption isotherms of Mg-Al-C catalysts show type II isotherm, demonstrating that the structure of Mg-Al-C catalysts is predominantly macroporous. The results of pore-size distribution diagram (**Fig. 1 f-g**) also show that the pore size of Mg-Al-C catalysts is mainly macroporous (60 nm-70 nm). Table 1 shows the specific surface area and pore properties parameters of Mg-Al-C catalysts. The results indicate that with the increase of Mg/Al loading ratios, the specific surface areas of Mg-Al-C catalysts change insignificant. Similarly, the results of Li et al point out that the changes in the loading amount of MgO/NaY hardly affect the specific surface area of the carbon-based substrate. Meanwhile, the BET surface area and pore size of Mg-Al-C catalysts are shown in **Table 1**. From Table 1, as the Mg loading amounts increase, the BET surface area of Mg-Al-C just remains between in 321.13 -387.04 $m^2 g^{-1}$. This result indicates that the increase in Mg loading amounts cannot significantly affect the specific area of the loaded substrate. Our previous work also pointed out that the increase of metal loading amount cannot evidently change the basic pore structure of biochar [35].

The XRD results of Mg-Al-C are shown in **Fig. 1h**. Based on the diffraction peak from XRD results, it is found that $_0$Mg-$_1$Al-C has no diffraction peak within the 2-Theta of 10-90°. The $_1$Mg-$_1$Al-C has relatively intensive diffraction peaks at 2-Theta of 36.9°, 42.9°, 62.3°, 74.7°, and 78.7°, respectively, which are attributed to the (111), (200), (220), (311) and (222) lattice planes of MgO crystals. The other Mg-Al-C catalysts also show similar results. The diffraction peak of MgO crystals in $_2$Mg-$_1$Al-C, $_3$Mg-

$_1$Al-C, $_4$Mg-$_1$Al-C, $_5$Mg-$_1$Al-C remains constant and just the peak area is increased with an increase Mg loading, indicating that the increase in Mg loading does not affect the stability of MgO crystal. The XRD results from Wang et al also illustrate that the loading amounts of Mg hardly affect the stability of MgO crystal phase [36]. As seen in the XRD results, no significant Al crystals diffraction peaks appear in the XRD pattern, and the Al^{3+} ion exhibits an amorphous or short-ordered crystalline state. This result should be due to the different preparation method and low carbonization temperature.

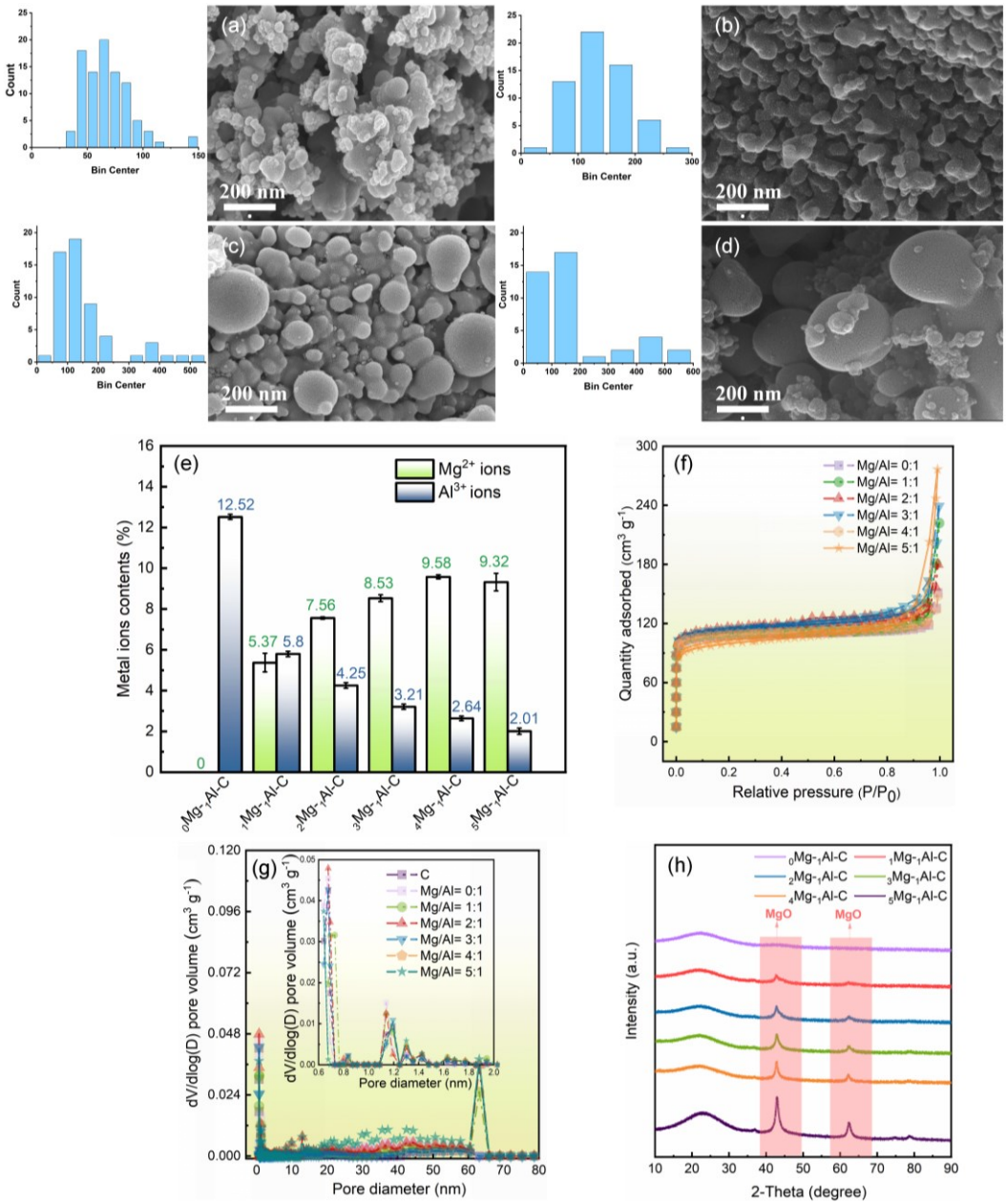

Fig. 1 SEM images of catalysts with different Mg/Al loading ratios: (**a**) $_1$Mg-$_1$Al-C, (**b**) $_2$Mg-$_1$Al-C, (**c**) $_3$Mg-$_1$Al-C, and (**d**) $_4$Mg-$_1$Al-C; (e) Mg^{2+} and Al^{3+} content in Mg-Al-C catalysts; (**f**) N_2 adsorption and desorption isotherms and (**g**) pore size distributions of Mg-Al-C (inset); (**h**) XRD spectra of Mg-Al-C.

Table 1. BET surface area and pore size of Mg-Al-C catalysts.

Samples	S_{BET} (m^2 g^{-1})	S_{micro} (m^2 g^{-1})	S_{micro}/S_{BET} (%)	Pore size (nm)
$_0$Mg-$_1$Al-C	321.13	286.22	89.13	2.91
$_1$Mg-$_1$Al-C	323.99	290.29	89.60	4.07
$_2$Mg-$_1$Al-C	351.02	286.78	81.70	3.17
$_3$Mg-$_1$Al-C	348.76	287.07	82.31	4.16
$_4$Mg-$_1$Al-C	330.20	290.14	87.87	2.78
$_5$Mg-$_1$Al-C	387.04	313.99	81.76	4.42

To further illustrate the primary bonding modes of Mg, Al and C, XPS analysis was performed on Mg-Al-C catalysts (**Figs 2, 3**). Four different compound valence bonding patterns occur on the Mg-Al-C catalysts surface identified by XPS, which are C 1*s*, O 1*s*, Mg 1*s*, and Al 2*p* peaks. The carbon groups were observed from **Fig. 2**: C-C/C=C (284.6 eV), C-OH/C-O-C (286.0 eV), and C=O (288.0 eV) [37]. In all the Mg-Al-C catalysts studied herein, four different oxygen groups were observed from **Fig. 2**: Mg-O (529.8 eV), Al-OH (531.5 eV), -O=C (531.6 eV), and C-OH/C-O-C (533.0 eV). From **Fig. 2**, it can be found that with the increasing of Mg/Al loading ratios, the ratio of peak area of C=C/CHx/C-C are maintained between 71.38-75.16%. This result also shows that the degree of graphitization of the Mg-Al-C catalyst is still high and has not changed significantly. Normally, the metal ions (Mg^{2+}, Al^{3+}) can be bonded with O, so the ratio of the peak area of C-OH/C-O-C deduces from 42.03% to 27.55% with the increasing of Mg/Al loading ratios. Simultaneously, the ratio of the peak area of Mg-O group increases from 13.36% to 30.90%. However, with the increasing of Mg/Al loading ratios, the total

loading amount of Al species decreases from 1/2 to 1/6, so the ratio of the peak area of Al-OH group decreases from 27.82% to 3.16%. This result illustrates that with the increasing of Mg/Al loading ratios, the more Mg-O group was formed on the Mg-Al-C catalyst surface than Al-OH group [38]. Additionally, two different Al groups are observed from Al 2*p* (**Fig. 3**), and the result indicates that Al on the catalysts surface is mainly present in the form of β-$Al(OH)_3$ and γ-$Al(OH)_3$ [20, 39]. Combined with the results of XRD, the two metal ions of Mg^{2+} and Al^{3+} are mainly present on the surface of the biochar in the form of MgO, β-$Al(OH)_3$, and γ-$Al(OH)_3$.

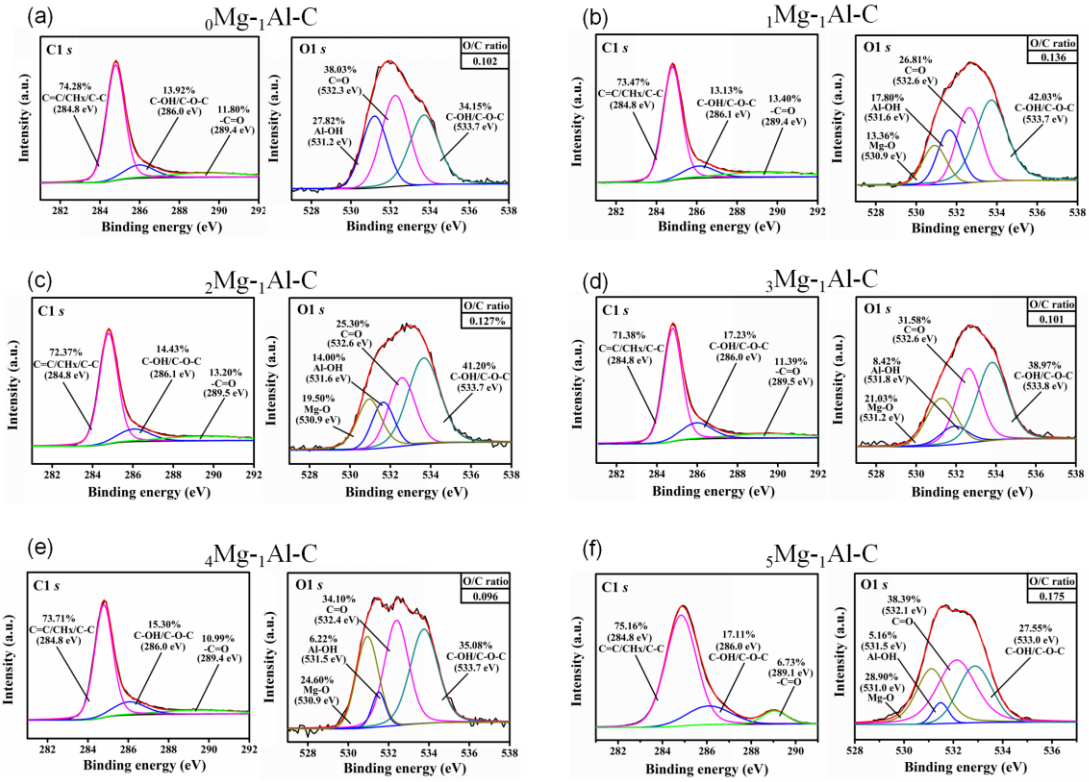

Fig. 2 C1*s* and O1*s* XPS peak results of Mg-Al-C catalysts with different Mg/Al loading ratios: (**a**) $_0$Mg-$_1$Al-C, (**b**) $_1$Mg-$_1$Al-C, (**c**) $_2$Mg-$_1$Al-C, (**d**) $_3$Mg-$_1$Al-C, (**e**) $_4$Mg-$_1$Al-C and (**f**) $_5$Mg-$_1$Al-C.

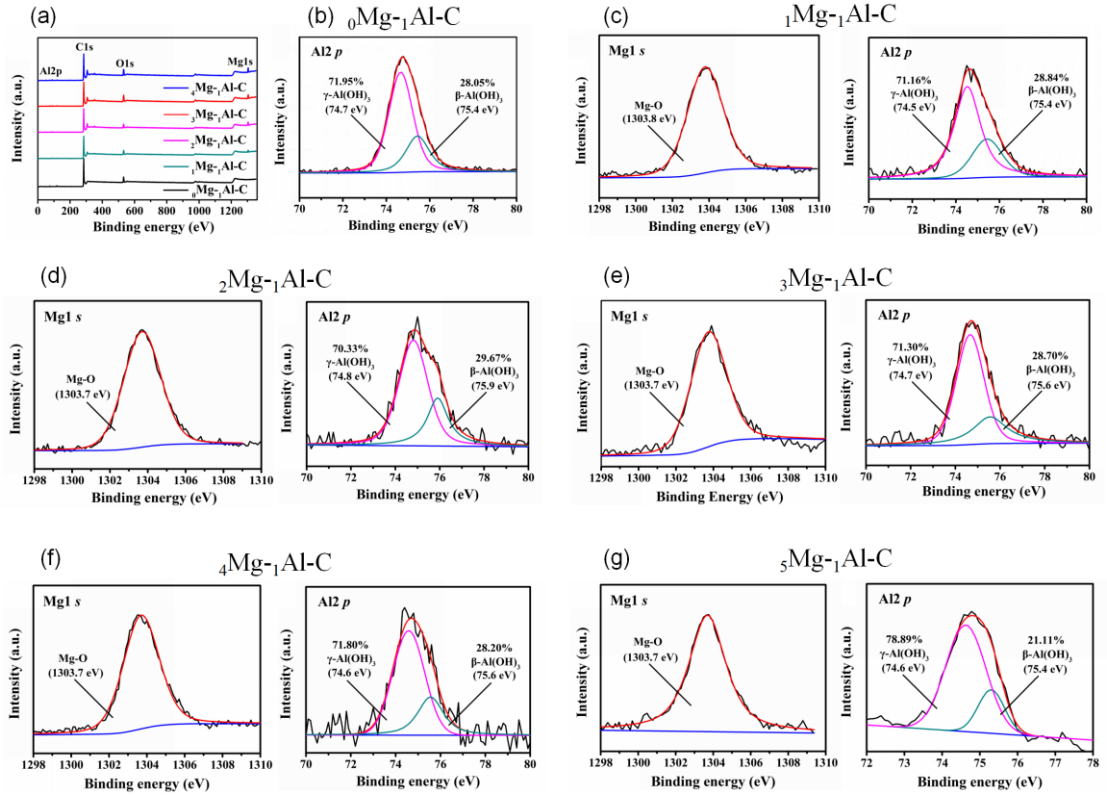

Fig. 3 Mg1*s* and Al2*p* XPS peak results of Mg-Al-C catalysts with different Mg/Al loading ratios: (**a**) full spectrum, (**b**) $_0$Mg-$_1$Al-C, (**c**) $_1$Mg-$_1$Al-C, (**d**) $_2$Mg-$_1$Al-C, (**e**) $_3$Mg-$_1$Al-C, (**f**) $_4$Mg-$_1$Al-C and (**g**) $_5$Mg-$_1$Al-C.

3.2 Catalytic performance and stability analysis of Mg-Al-C catalyst

The catalytic isomerization performance of Mg-Al-C with different Mg/Al loading ratios are shown in **Fig. 4**. From **Fig. 4a**, it can be found that the C only achieve a 2.21% glucose conversion rate. This is mainly because there is no active substance on the biochar surface that can catalyze the isomerization reaction of glucose. As the results of **Fig. 4a**, the only presence of Al amorphous structures (β-Al(OH)$_3$, γ-Al(OH)$_3$) in $_0$Mg-$_1$Al-C cannot achieve a high glucose conversion rate. This is because that both β-Al(OH)$_3$ and γ-Al(OH)$_3$ structures can accept the lone-pairs electrons to produce meta-aluminate ions and further inhibit the active sites to attack on glucose. In contrast, Sheng et al. inferred that other Al ions species include AlO(OH) and Al_2O_3 crystals could effectively catalyze the isomerization of glucose [40]. However, no significant Al crystals diffraction peaks (AlO(OH), Al_2O_3) appear in the XRD pattern,

thus leading to the low catalytic efficiency. As the Mg/Al loading ratios increase to 1:1, the $_1$Mg-$_1$Al-C catalytic glucose conversion rate raise to 18.8%. When the Mg/Al loading ratios increase to 4:1, the $_4$Mg-$_1$Al-C catalytic glucose conversion rate reaches to the maximum (31.5%). Combined with XPS and XRD results, it is inferred that the high conversion of glucose may be related to more Mg-O groups on the catalyst surface. Among the active sites, the MgO crystals could effectively catalyze the isomerization of glucose [39]. The reason is that the relatively high hydrolytic capacity of MgO (log K_b = 21.36) can generate numerous OH^- ions after hydrolysis, and the OH^- ions can cause homogeneous catalysis [39, 41].

Different with the $_0$Mg-$_1$Al-C, $_1$Mg-$_1$Al-C shows significant improvement in both selectivity and yield of fructose. As the Mg/Al loading ratios increase from 1:1 to 4:1, the selectivity and yield of fructose increase from 76.1% and 14.3% to 86.9% and 22.4%, respectively. When the Mg/Al loading ratios further increase to 5:1, the yield of fructose obtained from $_5$Mg-$_1$Al-C deduces to 20.08% due to the overloading of Mg. Based on the above results, it can be concluded that the optimal Mg/Al loading ratio is 4:1. Based on the above analysis, $_4$Mg-$_1$Al-C catalyst could achieve 86.99% fructose selectivity, 22.4% fructose yields, and 31.5% glucose conversion rate. However, the catalytic efficiency of $_4$Mg-$_1$Al-C catalyst is inferior to that of glucose isomerase [21]. To further optimize the catalytic efficiency of the $_4$Mg-$_1$Al-C catalyst, the $_4$Mg-$_1$Al-K-C catalyst was prepared to enhance the alkaline catalytic site.

The $_4$Mg-$_1$Al-C catalyst was reused, and the recycled catalyst was further characterized to investigate its stability (**Fig. 4b-c**). As shown in **Fig. 4b**, the glucose conversion rate and the fructose yield and selectivity were deteriorated continuously with an increase in reuse times. After the first use, the glucose conversion rate reduces from 31.5% to 10.6%, whereas the fructose yield and selectivity decrease from 86.1% and 22.4% to 21.6% and 3.81%, respectively. The XRD results (**Fig. 4c**) indicate that the peak

area of the MgO crystalline structure is significantly reduced. The MgO crystals almost completely disappear after the catalyst was used for the third time. The Mg^{2+} and Al^{3+} leaching rate of the $_4Mg\text{-}_1Al$-C catalyst during the reuse process is tested in order to further evaluate the stability of the catalyst, as shown in the **Fig. 4d**. The results demonstrate that in the $_4Mg\text{-}_1Al$-C-1 catalyst, the Mg^{2+} and Al^{3+} leaching amounts reach to 36.12% and 5.48%, respectively. As the reuse times increase, the leaching rate further increase. Meanwhile, the results also point out that the leaching amount of Mg^{2+} and Al^{3+}ions are much, which is the main problem of the poor stability of the Mg-Al-C catalyst.

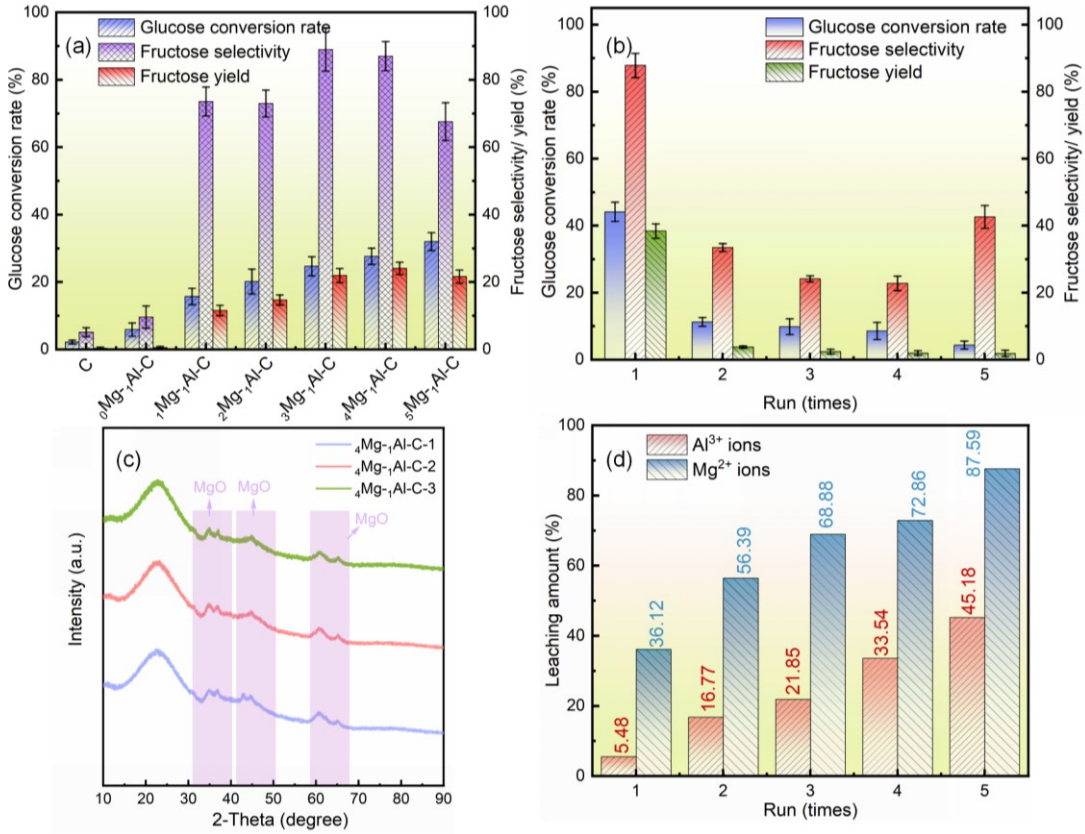

Fig. 4 Effects of different Mg-Al-C catalysts on the (**a**) catalytic efficiency; Effects of Mg-Al-C catalytic cycle times on (**b**) catalytic efficiency, (**c**) XRD spectra, and (**d**) Mg and Al ions leaching amount.

3.3 Characterization of Mg-Al-K-C catalyst

SEM images of Mg-Al-KCl-C, Mg-Al-KOH-C, Mg-Al-K_2CO_3-C, and Mg-Al-$KHCO_3$-C are shown in **Fig. 5a-d**.As with $_4$Mg-$_1$Al-C (**Fig. 1a-d**), the surface of Mg-Al-K-C catalysts have no obvious pores. No granular material was even observed on the surface of Mg-Al-K_2CO_3-C catalyst. The N_2 adsorption and desorption curves and pore-size distribution of Mg-Al-K-C catalysts with different K loading species are shown in **Fig. 5e-f**. According to the International Union of Pure and Applied Chemistry (IUPAC) classification of adsorption curves, the adsorption and desorption isotherms of Mg-Al-KCl-C show type I isotherms, illustrating that the structure of Mg-Al-KCl-C catalyst is predominantly microporous structure. The Mg-Al-KOH-C, Mg-Al-K_2CO_3-C, and Mg-Al-$KHCO_3$-C show type III isotherm, indicating the Mg-Al-KOH-C, Mg-Al-K_2CO_3-C, and Mg-Al-$KHCO_3$-C catalysts are mainly macroporous structure. The pore size distribution diagram of catalysts also demonstrates a macroporous structure in Mg-Al-KOH-C, Mg-Al-K_2CO_3-C, and Mg-Al-$KHCO_3$-C. **Table 2** shows the specific surface area and pore properties parameters of Mg-Al-K-C catalysts. Compared with the specific surface area of $_4$Mg-$_1$Al-C catalyst, the specific surface area of Mg-Al-KOH-C, Mg-Al-K_2CO_3-C, and Mg-Al-$KHCO_3$-C catalysts drop significantly from 330.20 $m^2\ g^{-1}$ to 7.10 $m^2\ g^{-1}$, 4.29 $m^2\ g^{-1}$, and 5.36 $m^2\ g^{-1}$. Combined with the results of SEM (**Fig.5(a-d)**) and XRD (**Fig. 5(g)**), some crystal substances of MgO, KCl, K_2CO_3 on the biochar surface were found after the loading of K, which covered some pores and resulted in the low surface area (**Table 2**). Our previous word pointed out the similar conclusion that the crystal substances of active materials are adsorb on the biochar surface will lead the surface area decreased from 416.16 m^2/g to 6.60 m^2/g [35]. On the other hand, compared to $_4$Mg-$_1$Al-C catalyst, the results in **Table 2** show that the pore size of Mg-Al-KOH-C, Mg-Al-K_2CO_3-C, and Mg-Al-$KHCO_3$-C catalysts increase from 2.78 nm to 26.08 nm, 14.78 nm, and 44.12 nm. This is because that the KOH, K_2CO_3, $KHCO_3$ further etch the surface of the biochar and enlarge the pore size after the loading of K. Similar results are

also obtained in the activation processing of carbon nanotubes by KOH etching (Liangliang Ji et al., 2010). It can be concluded that the load of the K-crystal structure will decrease the specific surface area of catalyst and increase the pore size of catalyst.

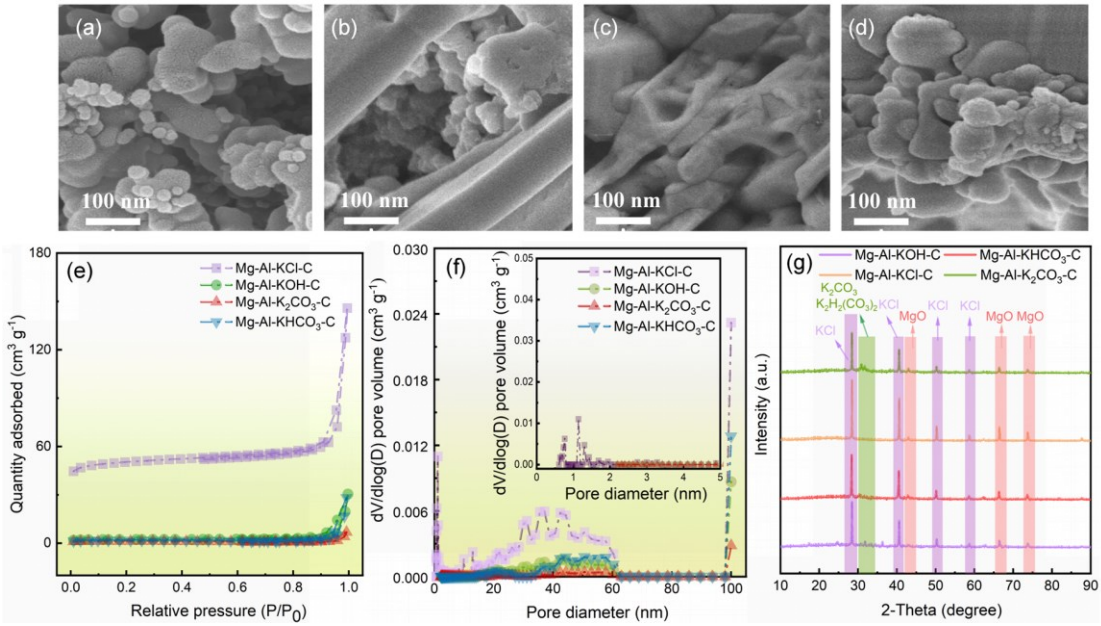

Fig. 5 SEM images of Mg-Al-K-C catalysts: (**a**) Mg-Al-KCl-C, (**b**) Mg-Al-KOH-C, (**c**) Mg-Al-K_2CO_3-C, (**d**) Mg-Al-$KHCO_3$-C; (**e**) N_2 adsorption and desorption isotherms and (**f**) pore size distributions of Mg-Al-K-C (inset); (**g**) XRD spectra of Mg-Al-K-C.

Table 2. BET surface area and pore size of Mg-Al-K-C catalysts.

Samples	S_{BET} ($m^2\ g^{-1}$)	S_{micro}($m^2\ g^{-1}$)	S_{micro}/S_{BET} (%)	Pore size (nm)
Mg-Al-C	330.20	290.14	40.06	2.78
Mg-Al-KCl-C	193.56	161.88	31.68	4.66
Mg-Al-KOH-C	7.10	6.71	0.39	26.08
Mg-Al-K_2CO_3-C	4.29	2.85	1.44	14.78
Mg-Al-$KHCO_3$-C	5.36	3.96	1.40	44.12

The XRD results of Mg-Al-K-C are shown in **Fig. 5g**. Based on the diffraction peak from XRD results, it is found that these Mg-Al-K-C catalysts have relatively intensive diffraction peaks at 2-Theta of 36.9°,

42.9°, 62.3°, 74.7°, and 78.7°, attributed to the (111), (200), (220), (311), and (222) lattice planes of MgO crystals [42]. In **Fig. 5g**, the Mg-Al-KCl-C only contains KCl and MgO crystals. Moreover, in contrast to Mg-Al-KCl-C, Mg-Al-KOH-C, and Mg-Al-K_2CO_3-C, the Mg-Al-$KHCO_3$-C mainly contains KCl, MgO and a few K_2CO_3, $K_4H_2(CO_3)_3$ crystals. The co-impregnation process promotes the reordering and migration of KCl, K_2CO_3, $K_4H_2(CO_3)_3$ crystalline structures [43]. **Fig. 6** shows that the binding energy of Mg 1*s* and Al 2*p* peak shifts in different Mg-Al-K-C catalysts. In all the catalysts studied herein, two different groups are observed from Mg 1*s* peak in **Fig. 6**: Mg-O (1303.8 eV) and $MgCO_3$ (1305.0 eV). The results indicate that Mg-Al-KCl-C only has an Mg-O structure (at 1303.8 eV). $MgCO_3$ (1305.0 eV) was also present in Mg-Al-KOH-C, Mg-Al-K_2CO_3-C, and Mg-Al-$KHCO_3$-C with the diffraction peak areas of 42.29%, 41.38%, and 30.58%, respectively. Meanwhile, two different groups are observed from Al 2*p* peak in **Fig. 6** : β-$Al(OH)_3$ (75.8 eV) and γ-$Al(OH)_3$ (74.4 eV). Due to the electrostatic potential field, the Al 2*p* binding energies shifts among oxides, hydroxides, and oxyhydroxides. However, the O/Al atom ratio is as high as 13.00 for Mg-Al-KOH-C catalyst when the KOH co-impregnation (Table 3). This high ratio of O/Al for Mg-Al-KOH-C catalysts provides many oxygen vacancies and unsaturated catalysis sites, which benefits the glucose isomerization.

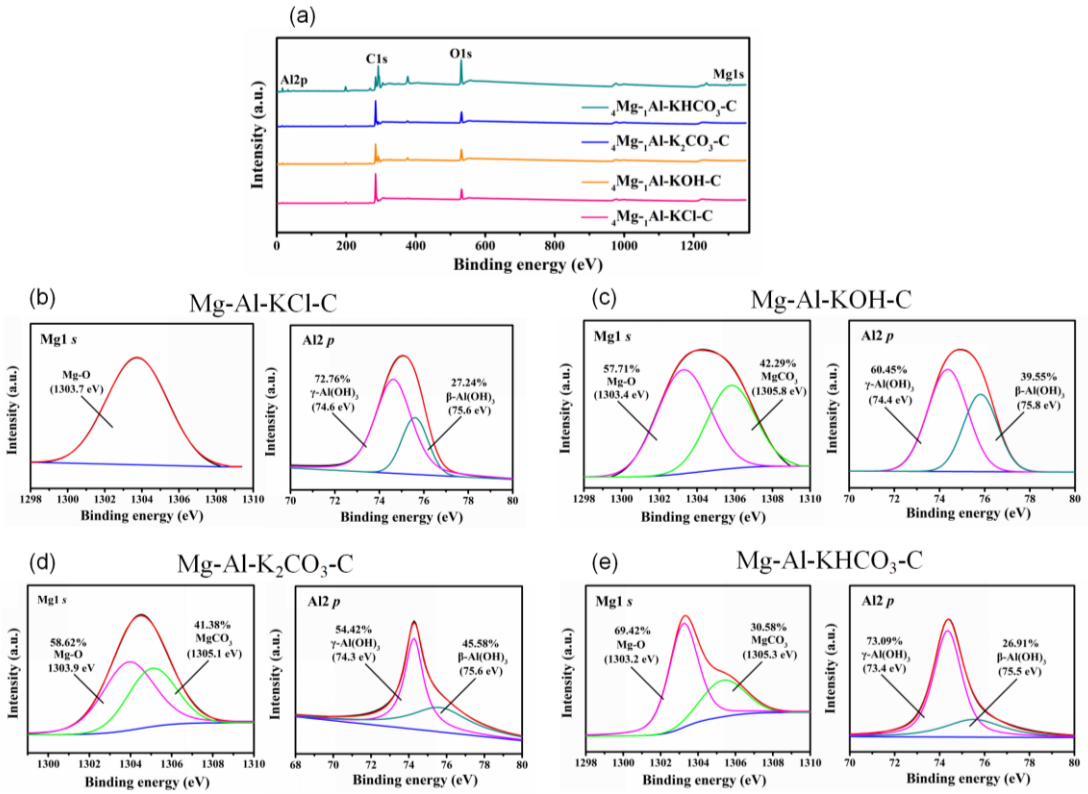

Fig. 6 Mg1*s* and Al2*p* XPS peak results of Mg-Al-K-C catalysts: (**a**) full spectrum, (**b**) Mg-Al-KCl-C, (**c**) Mg-Al-KOH-C, (**d**) Mg-Al-K_2CO_3-C, (**e**)Mg-Al-$KHCO_3$-C.

Table 3. C 1s, O 1s, Mg 1s, Al 2p peak results of Mg-Al-K-C catalysts from XPS.

Samples	Atoms (%)				O/Al	O/Mg
	C1*s* (%)	O1*s* (%)	Mg1*s* (%)	Al2*p* (%)		
Mg-Al-KCl-C	72.1%	19.33%	4.12%	4.45%	4.30	4.70
Mg-Al-KOH-C	58.90%	30.58%	8.17%	2.35%	13.00	3.70
Mg-Al-K_2CO_3-C	67.55%	23.87%.	6.55%	2.03%	11.70	3.90
Mg-Al-$KHCO_3$-C	55.98%	35.21%	6.18%	2.63%	13.38	4.10

3.4 Catalytic performance and stability of Mg-Al-K-C catalyst

The catalytic performance of the Mg-Al-K-C catalysts is evaluated, and the results are shown in **Fig. 7**. Compared with $_4$Mg-$_1$Al-C, the glucose conversion rate of Mg-Al-KOH-C, Mg-Al-K_2CO_3-C, and Mg-Al-$KHCO_3$-C catalysts increases from 27.64% to 42.88%, 41.56%, and 44.12%, respectively, while the

glucose conversion rate of Mg-Al-KCl-C catalyst reduces from 27.64% to 19.76%. This is because that lots of basic active sites (e.g., MgO, $K_4H_2(CO_3)_3$, K_2CO_3) were formed in Mg-Al-KOH-C, Mg-Al-K_2CO_3-C (**Fig. 5g**), and Mg-Al-$KHCO_3$-C catalysts during preparation progress, thus increasing catalytic efficiency and improving glucose conversion rate and fructose yield. Meanwhile, **Table 3** shows that, the value of O/Al for Mg-Al-$KHCO_3$-C is as high as 13.38, which will provide many oxygen vacancies and unsaturated acidic catalysis sites and benefit glucose isomerization. Similarly, the improvement reason of glucose conversion efficiency for Mg-Al-KOH-C and Mg-Al-K_2CO_3-C is the same. The reduction in glucose conversion rate caused by Mg-Al-KCl-C catalyst is due to the presence of KCl crystal in the catalyst (**Fig. 7g**), compared with the $_4$Mg-$_1$Al-C (only MgO crystal). Combined with the catalyst's morphology (**Fig. 5a-c**), the KCl crystal encapsulates $Al(OH)_3$ and hinders the dissolution of OH^- ions, thus deteriorating the efficiency of $Al(OH)_3$ attacking on glucose and reducing glucose protonation. Meanwhile, the fructose yield of the Mg-Al-K-C catalysts are shown in **Fig. 7a**. The results shows that Mg-Al-KOH-C, Mg-Al-K_2CO_3-C, and Mg-Al-$KHCO_3$-C catalysts can reach a 31.27%, 36.95%, and 38.37% fructose yield higher than Mg-Al-C (24.05%). However, due to the low glucose conversion rate of Mg-Al-KCl-C catalyst (19.76%), the Mg-Al-KCl-C catalyst just can obtain a 19.51% fructose yield. Compared to other catalysts, the Mg-Al-$KHCO_3$-C not only could obtain a higher glucose conversion rate (44.12%), but also obtain a higher fructose yield (38.37%).

The fructose selectivity trends of the Mg-Al-K-C catalysts are different with the glucose conversion rate. As follow, the fructose selectivity can reach 98.69% during the Mg-Al-KCl-C catalytic process. However, the fructose selectivity of Mg-Al-KOH-C, Mg-Al-K_2CO_3-C, and Mg-Al-$KHCO_3$-C is 69.68%, 83.01%, and 87.82%, respectively. From the perspective of basic catalysis sites, the high selectivity of Mg-Al-KCl-C is explained by the fact that the content of MgO in Mg-Al-KCl-C reaches to 100% (**Fig.**

6). While the MgO contents of Mg-Al-KOH-C, Mg-Al-K_2CO_3-C, and Mg-Al-$KHCO_3$-C is 57.71%, 58.62%, and 69.42%, respectively. This is because high content of MgO in Mg-Al-KCl-C catalyst can react with the H_2O to produce the more OH^- ions than other catalyst with low content of MgO, and the OH^- ions are favourble to isomerization reaction. From the perspective of acidic catalysis sites, **Table 3** shows that the maximum value of O/Mg can been found in Mg-Al-KCl-C catalyst for 4.7. These results point out that high O/Mg ratio affects the selectivity of glucose isomerization to fructose. This is because under the same total loading amount, the high O/Mg ratio can provide more oxygen-unsaturated sites to improve the fructose selectivity than low O/Mg ratio. Thus, second only to Mg-Al-KCl-C, the Mg-Al-$KHCO_3$-C also has a high selectivity for fructose. In addition to the effect of Mg elements, the reason for the high fructose selectivity in Mg-Al-KCl-C catalyst is the presence of $Al(OH)_3$ or $[Al(OH)_2(aq)]^+$, because Lewis acid catalysis active sites can be beneficial to obtain highly fructose selectivity [44]. The XPS results from **Table 3** also shows that the content of Al 2*p* peak (4.45%) in Mg-Al-KCl-C higher than Mg-Al-KOH-C (2.35%), Mg-Al-K_2CO_3-C (2.04%) and Mg-Al-$KHCO_3$-C catalyst (2.63%). It is important to note that the fructose selectivity (70.0%-88.0%) obtained from Mg-Al-KOH-C, Mg-Al-K_2CO_3-C and Mg-Al-$KHCO_3$-C still has a high level than others in the isomerization catalyst [19, 44]. These results suggest that adding crystalline and amorphous active sites in catalysts by co-impregnating can preserve high fructose selectivity while increasing glucose conversion rate to fructose. Based on the above analysis, it is concluded that the Mg-Al-$KHCO_3$-C has better catalytic efficiency than other catalysts.

The Mg-Al-$KHCO_3$-C catalyst was reused, and its catalytic performance was investigated in order to evaluate its stability. The glucose conversion rate and selectivity of fructose decrease with an increase in the reuse times **(Fig. 7 b)**. When the catalyst is twice used, the glucose conversion rate decreases from

36.86% to 29.78%, and the yield and selectivity of fructose decrease from 32.37% to 14.27% and from 87.82% to 49.38%, respectively. As shown in **Fig. 7c**, the XRD spectra of the Mg-Al-$KHCO_3$-C catalyst after its first uses reveals the disappearance of the MgO, K_2CO_3, and $K_4H_2(CO_3)_3$ diffraction peaks. Furthermore, compared to Mg-Al-C-1 catalysts, in the Mg-Al-$KHCO_3$-C-1 catalysts Al_2O_3 new crystalline peaks appear at 2-Theta of 36.5°, 45.5°, and 66.4° after first uses. Combined with the analysis of **Table 3**, we infer that the reason for this result is that the low content of Al species in Mg-Al-K-C catalysts is due to Al_2O_3 diffraction peak being overlapped by other diffraction peaks. Meanwhile, when MgO, K_2CO_3, and $K_4H_2(CO_3)_3$ in Mg-Al-$KHCO_3$-C are leached, only Al_2O_3 structure still exists. Thus, the dissolution of active sites in Mg-Al-K-C catalysts may contribute their negative stability.

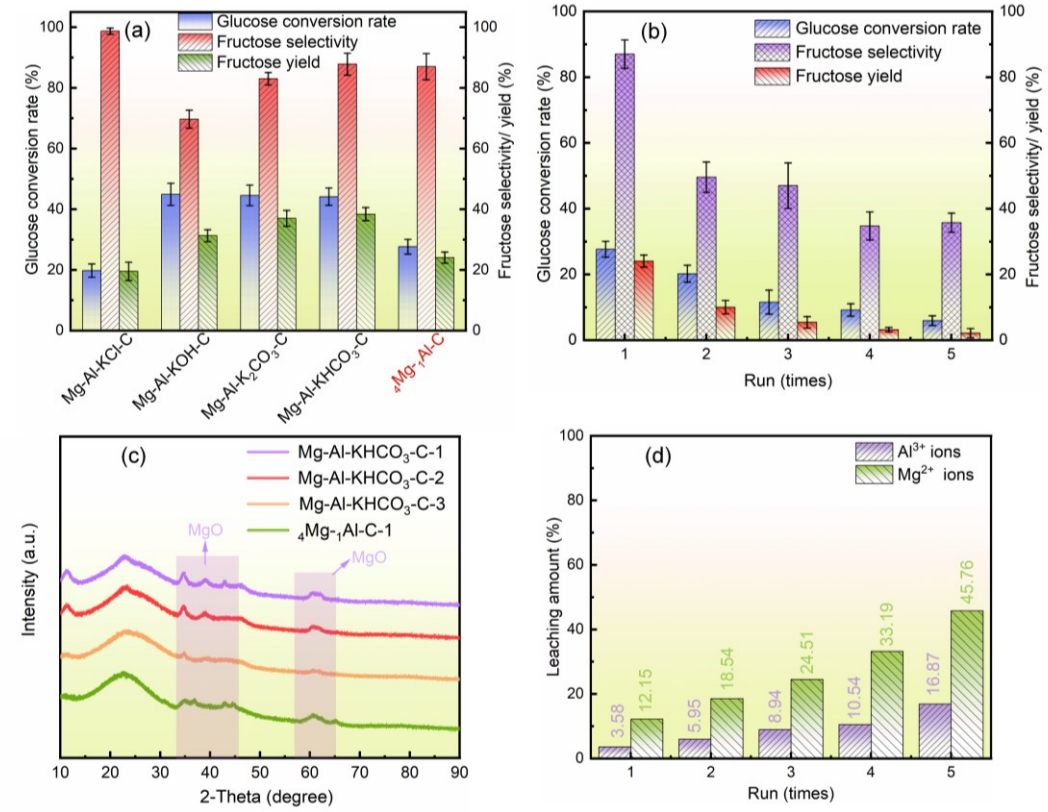

Fig. 7. Effects of different Mg-Al-K-C catalysts on the (**a**) catalytic efficiency; Effects of Mg-Al-$KHCO_3$-C catalytic cycle times on (**b**) catalytic efficiency, (**c**) XRD spectra, and (**d**) Mg and Al ions leaching amounts.

3.5 Catalytic mechanism

The catalytic performance of different biochar-based metal catalysts is summarized in **Table 4**. The 25~30% fructose yield, 70-93% fructose selectivity, and 20%-40% glucose conversion rate are obtained using the reported biochar-based metal catalysts. In this study, 38.37% fructose yield, 87.8% fructose selectivity, and 44.12% glucose conversion rate are achieved using the Mg-Al-$KHCO_3$-C catalyst, which is higher than most reported catalysts, particularly in the fructose yield and glucose conversion rate [19, 20, 26, 40, 42, 44].

Table 4. Catalytic efficiency comparison of different biochar-based metal catalysts on glucose isomerization.

Catalysts	References	Catalytic conditions (solvent)	Fructose yield (%)	Glucose conversion rate (%)
$N_{0.5}/HC_{240}$-RO_{400}	[44]	120 ℃, 45 min (H_2O)	31.10	32-38.00
CS-CaO-800	[40]	80 ℃, 40 min (H_2O)	29.20	40.90
20%Al-500N_2	[20]	160 ℃, 20 min (Acetone/H_2O)	21.50	20-40.00
HC_{200}-$Al_{10\%}$-$KHCO_3$	[19]	160 ℃, 20 min (H_2O)	32.60	34.10
Al/HC-300	[26]	160 ℃, 20 min (Acetone/H_2O)	24.40	31-35.00
EG-MgO-BC-600-N_2	[42]	100 ℃, 20 min (H_2O)	30.00	-
$_4$Mg-$_1$Al-C*	**This work**	**100 ℃, 30 min**	**22.40**	**31.50**
Mg-Al-$KHCO_3$-C*	**This work**	**(H_2O)**	**38.37**	**44.12**

Based on previously researchers, the loaded active materials and their synergism are the key factors to influence the efficiency of catalyze, which also are consistent to many studies [39, 45, 46]. The $Al(OH)_3$, MgO, KCl, $K_4H_2(CO_3)_3$ are considered as important active materials that provide multi-catalytic sites for glucose isomerization [25, 47]. Different catalytic active materials are present at the same time in an efficient catalyst, thus the synergies between active materials need to be further clarified. In this study, as the Mg/Al loading ratio increases to 4:1, the $_4$Mg-$_1$Al-C catalytic glucose conversion rate reaches to 26.6%. The catalytic results of $_4$Mg-$_1$Al-C have confirmed the role of MgO (**Fig. 1d and 3**). From **Fig. 7**, based on the multi-catalytic efficiency of the Mg-Al-KCl-C catalyst containing KCl and MgO crystals and the Mg-Al-C catalyst containing MgO crystals, it is concluded that the synergism of KCl and MgO crystals leads to a decrease in the catalytic efficiency of glucose isomerization. The main reason for this result is that the addition of KCl reduce the pore size of the Mg-Al-KCl-C (**Table 2**), wrapping the active sites MgO inside, making it difficult to access glucose for catalysis. In our previous work, the isomerization effect of KCl on glucose have been clarified [35]. The Mg-Al-$KHCO_3$-C has excellent catalytic efficiency than Mg-Al-KCl-C. In the co-impregnation and pyrolysis process in the preparation of Mg-Al-$KHCO_3$-C, the interaction of $MgCl_2$, $AlCl_3$ and $KHCO_3$ with biochar promotes the reordering and migration of Mg, Al, and K species [43], resulting in the formation of some material species such as MgO, $Al(OH)_3$, KCl, and $K_4H_2(CO_3)_3$. The catalytic efficiency of Mg-Al-$KHCO_3$-C on glucose may been determined together by these active materials. Different with the catalytic efficiency of Mg-Al-KCl-C, the synergism effects of the $Al(OH)_3$ and the KCl, MgO, $K_4H_2(CO_3)_3$ crystals in Mg-Al-$KHCO_3$-C lead to an increase in catalytic efficiency of glucose isomerization, the fructose yield can reach 38.37%. This is because the $K_4H_2(CO_3)_3$ increases the pore size of the Mg-Al-$KHCO_3$-C catalyst during the pyrolysis process (**Table 2**), thereby increasing the contact between active substances

($Al(OH)_3$, MgO) and glucose. The pore structures of Mg-Al-$KHCO_3$-C can be found in the SEM image at different scales, as shown in **Fig. S2**. Meanwhile, the XPS results from **Table 3** shows that, the value of O/Al for Mg-Al-$KHCO_3$-C is as high as 13.38, which will provide many oxygen vacancies and unsaturated acidic catalysis sites, benefiting the glucose isomerization [48]. In order to further demonstrate the function of MgO and $Al(OH)_3$, the acidity and basicity of Mg-Al-$KHCO_3$-C is determined by temperature programmed TPD-NH_3 and TPD-CO_2. **Fig. S1** shows that the peak of basic sites from Mg-Al-C-CO_2 appears at 99.6 ℃ and 427.9 ℃, and that of Mg-Al-$KHCO_3$-C-CO_2 appears at 104.2 ℃ and 395.8 ℃ [20]. When only MgO and $Al(OH)_3$ active sites appear on Mg-Al-C, the catalyst surface emerges strongly basic (T= 427.9 ℃ > 400 ℃). While the presence of MgO, $Al(OH)_3$, $K_4H_2(CO_3)_3$ on the surface of Mg-Al-$KHCO_3$-C leads to weakly basic (T= 395.8 ℃ < 400 ℃) . In our previous work, the basic materials could improve the glucose conversion rate [35]. Similar with our previous work, from the results of catalytic efficiency, weakly basic materials are beneficial to improve catalytic efficiency. Furthermore, the quantity of weakly basic materials of Mg-Al-$KHCO_3$-C (271.6 μmol/g) is higher than the strongly basic of Mg-Al-C (251.4 μmol/g). From the perspective of acidic active materials, the peak of acid materials from Mg-Al-C-NH_3 appears at 105.5 ℃ and 435.2 ℃, and that of Mg-Al-$KHCO_3$-C-NH_3 emerges at 107.1 ℃ and 395.1 ℃ [20]. Similarly, only MgO and $Al(OH)_3$ active materials appear on the surface of $_4$Mg-$_1$Al-C, the catalyst surface shows strongly acid (T= 435.2 ℃ > 400 ℃) [49]. While the presence of MgO, $Al(OH)_3$, $K_4H_2(CO_3)_3$ from Mg-Al-$KHCO_3$-C leads to weakly acid (T= 395.1 and 107.1 ℃ < 400 ℃). From the results of catalytic efficiency, weakly acid materials are beneficial to improve fructose selectivity than strongly acid materials. Furthermore, the quantity of weakly acidic materials in Mg-Al-$KHCO_3$-C (156.5 μmol/g) is higher than that of $_4$Mg-$_1$Al-C (66.7 μmol/g), leading to the fructose selectivity of Mg-Al-$KHCO_3$-C better than that of Mg-Al-

C. The above results show that the properties and quantity of active materials in catalyst are important to achieve high glucose conversion rate and fructose selectivity. However, it is still unclear why the weakly acidic materials improve fructose selectivity and the synergistic effect of acidic and basic active materials on the catalytic efficiency. Therefore, we hope to expound the intermediate structure formed during catalytic process by calculating the kinetics and thermodynamics data of reaction with density functional theory (DFT) in order to further clarify the main reaction pathways.

From the above experimental analysis results, it was found that main active sites (MgO, $Al(OH)_3$) in Mg-Al-$KHCO_3$-C could catalyze the glucose isomerize to fructose. However, the catalytic mechanism of these active materials can not fully elucidate these results. The M06-2X function, combined with the TZVP basis set, was adopted for the calculation of kinetics and thermodynamics data of reaction in order to further explain the Brønsted basic and Lewis acid catalytic mechanism. The solvation of water was referenced to the SMD solvation model. The zero point of the proton was taken as H_3O^+ in water.

Based on above results, we calculated the energy of initial reactants (glucose), intermediates, and final reactant (fructose) in the Brønsted basic and Lewis acid catalytic process. In the Brønsted basic and Lewis acid catalytic pathway, the initial reactants (glucose) is considered as a reference energy point. As shown in **Fig. 8**, the quantum chemical calculation results and geometric optimization configuration in the Brønsted basic and Lewis acid catalytic pathway are obtained. In **Fig. 8a**, the key rate-limiting step in Brønsted basic catalytic pathway is the optimize-structure of acyclic glucose (TS3-1), which undergoes keto-enol tautomerism through imtermediate 3 (IM3) to form an acyclic fructose (A3) under an energy barrier of 26.7 kcal/mol. Meanwhile, in Brønsted basic catalytic pathway， the glucose (A1) undergoes ring-opening reaction to form acyclic glucose (IM2) under an energy barrier of 16.8 kcal/mol. From **Fig. 8b**, the key rate-limiting step in Lewis acid catalytic pathway is that the glucose (A1)

undergoes ring-opening reaction through intermediate 1 (B1) to form an acyclic glucose (IM2) under an energy barrier of 22.1 kcal/mol. Simultaneously, in Lewis acid catalytic pathway, the glucose (A1) undergoes ring-opening reaction to form acyclic glucose (IM2) under an energy barrier of 17.9 kcal/mol. This result shows that Brønsted basic materials (16.8 kcal/mol) have a great effect on the ring-opening reaction to form acyclic glucose than Lewis acid materials (22.1 kcal/mol). While, Lewis acid materials (17.9 kcal/mol) have a great effect on promoting acyclic glucose isomerize to form fructose than Brønsted basic materials (26.7 kcal/mol). Meanwhile, this results also indicate that acid materials ($Al(OH)_3$) are beneficial to improve fructose selectively, and basic sites (MgO) are beneficial to improve glucose conversion rate. From the above results (**Fig. 4a, 7a**), it is pointed out that the best catalytic efficiency in Mg-Al-C and Mg-Al-$KHCO_3$-C could be achieved when the Mg/Al loading ratio on the catalyst is 4:1. The main reason is due to the collaboration of MgO and $Al(OH)_3$. From the results of DFT, the collaboration between MgO and $Al(OH)_3$ is mainly conducted through the hydroxylation of MgO, providing OH^- ions for the ring-opening reaction of cyclic glucose to form acyclic glucose. Continually, the $Al(OH)_3$ sites interact with the carbonyl groups on acyclic glucose and coordinate with acyclic glucose on the C1-O and C2-O positions to initiate the intramolecular hydride shift. When the Mg/Al ratio continually increases from 4:1 to 5:1, the catalytic efficiency of Mg-Al-C gradually decreases (**Fig. 4a**). The reason is that, the excess loaded MgO dominates the Brønsted basic isomerization reaction. During MgO promoting acyclic glucose isomerize to form fructose, it need to overcome 26.7 kcal/mol energy barrier, which is higher than $Al(OH)_3$ (17.9 kcal/mol). Meanwhile, the excess loaded MgO can attack fructose to isomerize back to glucose [35]. This point will be further analyzed in the section on the molecular surface electrostatic potential (ESP). Therefore, in order to

improve the catalytic efficiency, it is need to design a catalyst that contains both Lewis acid and Brønsted basic catalytic active materials and need to be loaded with a suitable Mg/Al ratio.

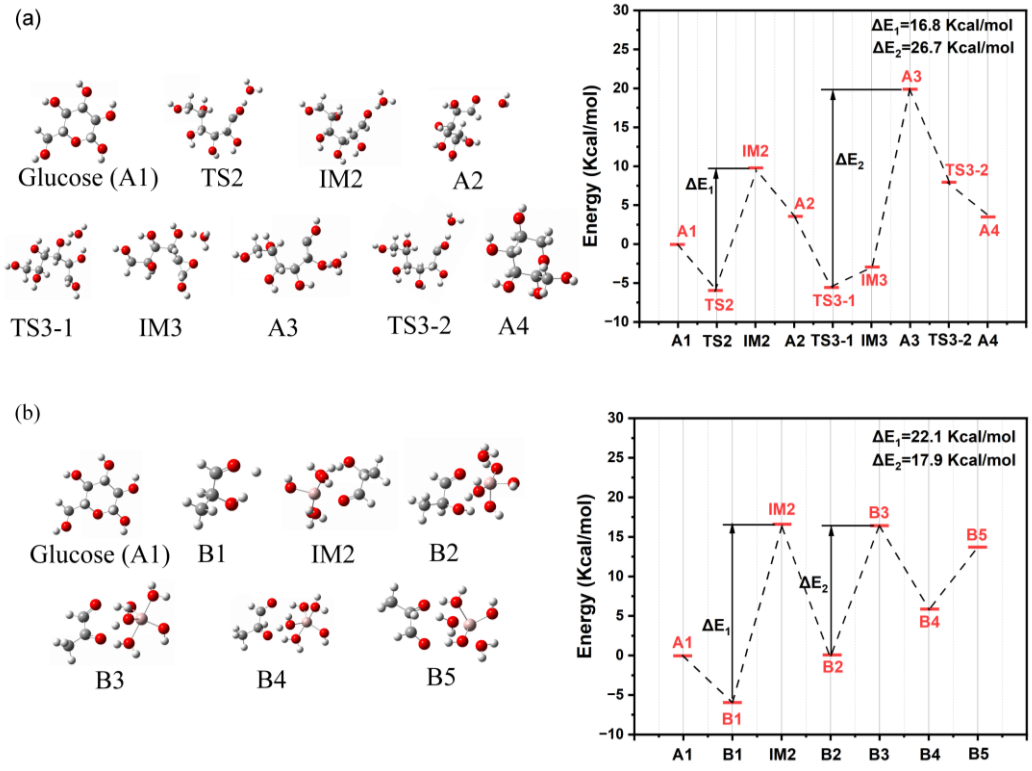

Fig. 8 Quantum chemical calculations and geometric optimization configuration of glucose isomerization under (**a**) Brønsted basic and (**b**) Lewis acid catalyst.

It is known from current research that during chemical molecular reactions, non-covalent interactions between molecules contribute to the occurrence of chemical reactions . The non-covalent interaction analysis was performed using interaction region indicator (IRI) method to illustrate the interface interaction between the glucose and active materials [50]. The non-covalent interaction mainly exists in between acyclic glucose and H_2O, acyclic glucoses, acyclic glucose and $Al(OH)^{3+}$, and acyclic fructose and $Al(OH)^{3+}$(**Fig. 9**). From **Fig. 9a**, the results show that the non-covalent interaction exists in the deprotonation materials of acyclic glucose due to the hydrogen bonding interaction (blue area in iso-surfaces). The volume of the interacting regions can be taken as an indication of the extent of interaction. Among, as the volume of the interacting regions increases, the interaction strength will be enhanced.

Meanwhile, van der Waals interaction (green area in iso-surfaces) exists in between the acyclic glucose of C2 and C6 (**Fig. 9b**). In the **Fig. 9c**, it can be seen that extensive non-covalent interaction occurs between the acyclic glucose and $Al(OH)_3$ due to the hydrogen bonding interaction and van der Waals interaction. Additionally, the results from **Fig. 9d** show the similar results that extensive hydrogen bonding interaction and van der Waals interaction appear between the acyclic fructose and $Al(OH)_3$. In summary, the above results demonstrate that the interaction between H_2O and acyclic glucose during Brønsted basic isomerization process only relies on hydrogen bond. In contrast, the interaction between $Al(OH)^{3+}$ and acyclic glucose during Lewis acid isomerization process not only relies on hydrogen bond, but also relies on van der Waals interaction. This also proves the conclusion of **Fig. 8** that Lewis acid materials (17.9 kcal/mol) have a great effect on promoting acyclic glucose isomerize to form fructose than Brønsted basic materials (26.7 kcal/mol).

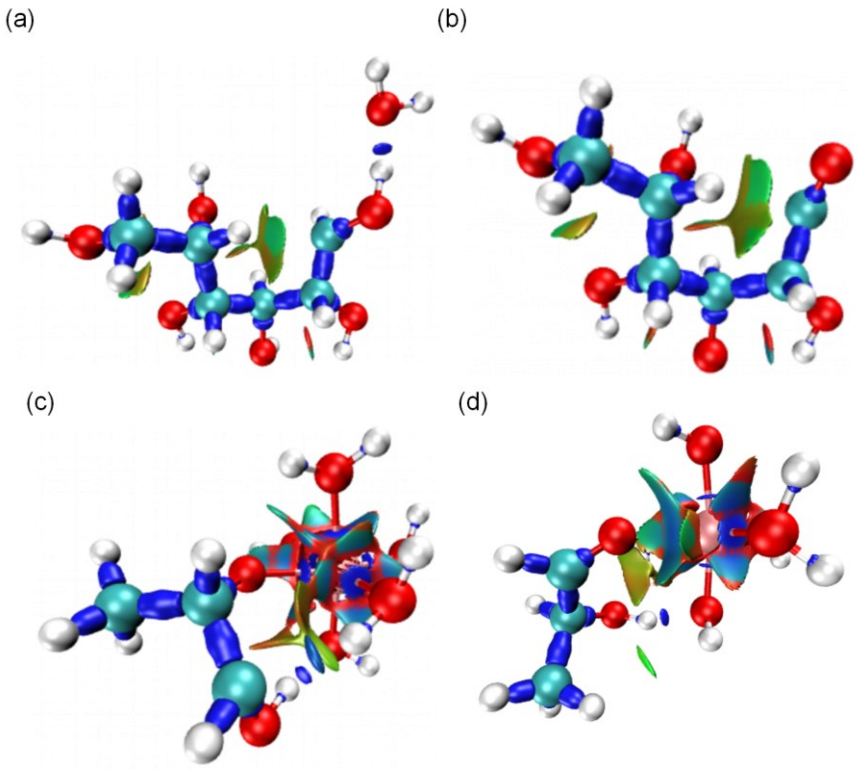

Fig. 9 The ` exists in between (**a**) acyclic glucose and H_2O, (**b**) acyclic glucoses, (**c**) acyclic glucose and $Al(OH)^{3+}$, and (**d**) acyclic fructose and $Al(OH)^{3+}$. Different iso-surfaces are colored according to BGR scheme during the electron density range −0.05 a.u. < sign(λ2) ρ < 0.05 a.u.

During chemical molecular reactions, the electrostatic interaction is the premise to promote the reaction occurring, particularly clear in the molecular surface electrostatic potential (ESP). In this study, in addition to the non-covalent interaction analysis, the molecular surface ESP analysis of the transition states is also performed. Firstly, four intermediates including (TS2, TS3-2, B2, B5) in **Fig. 8** were molecular optimized, and the data were analyzed using Multiwfn 3.8 wave function analysis software [51]. Among, TS2, TS3-2, B2, and B5 are attributed to the intermediate of acyclic glucose and H_2O, acyclic fructose and H_2O, acyclic glucose and $Al(OH)^{3+}$, and acyclic fructose and $Al(OH)^{3+}$, respectively. Combined with Visual Molecular Dynamics (VMD), the molecular surface ESP distribution map was plotted [52]. The quantitative distribution of the molecular surface ESP of above four intermediates are shown in **Fig. 10**. From **Fig. 10a**, the O9 is the main electron-absorbing group, which are distributed in the blue region, and easily attacked by electrophiles. As seen from **Fig. 10b**, when basic active site is existed, H_2O distributes in the red region and acts as an electron donating group. Moreover, there is a potential difference between the hydroxyl group at O9 from TS3-2, and it is easily to obtain electrons from H_2O. Additionally, this is also the main reason why acyclic fructose is attacked by excess active sites (MgO) in Brønsted basic environment. Combining with the results of **Figs. 8-10**, the results pointe out that the presence of MgO is beneficial to improve glucose conversion rate, but excess MgO will also cause fructose to re-isomerize into glucose and reduce the fructose selectivity. Therefore, it is important to rationally design the loading amount of Brønsted basic sites (MgO) in a catalyst.

Further, the key intermediates of ESP distributions in Lewis acid environment is analyzed. **Fig. 10c** shows the ESP distributions of key intermediates composed of B2 under Lewis acid catalysis. From the

quantitative distribution of the molecular surface ESP, the difference of molecular surface ESP between $Al(OH)_3$ and acyclic glucose is low, while the difference between $Al(OH)_3$ and acyclic fructose is high, which illustrate that $Al(OH)_3$ acts as an electron donating groups are more likely to attack the hydroxyl groups of acyclic fructose, but not acyclic glucose. This also proves that the initial designed catalyst loading a low proportion of Lewis acidic sites is reasonable. Meanwhile, compared with Brønsted basic catalysis **(Fig. 10a-b)**, the ESP difference between the active materials and acyclic glucose is larger under Lewis acid catalysis (**Fig. 10c-d**), and the acyclic glucose is more susceptible to being attacked by the Lewis acid active materials. This is similar to the conclusion obtained in **Fig. 8**.

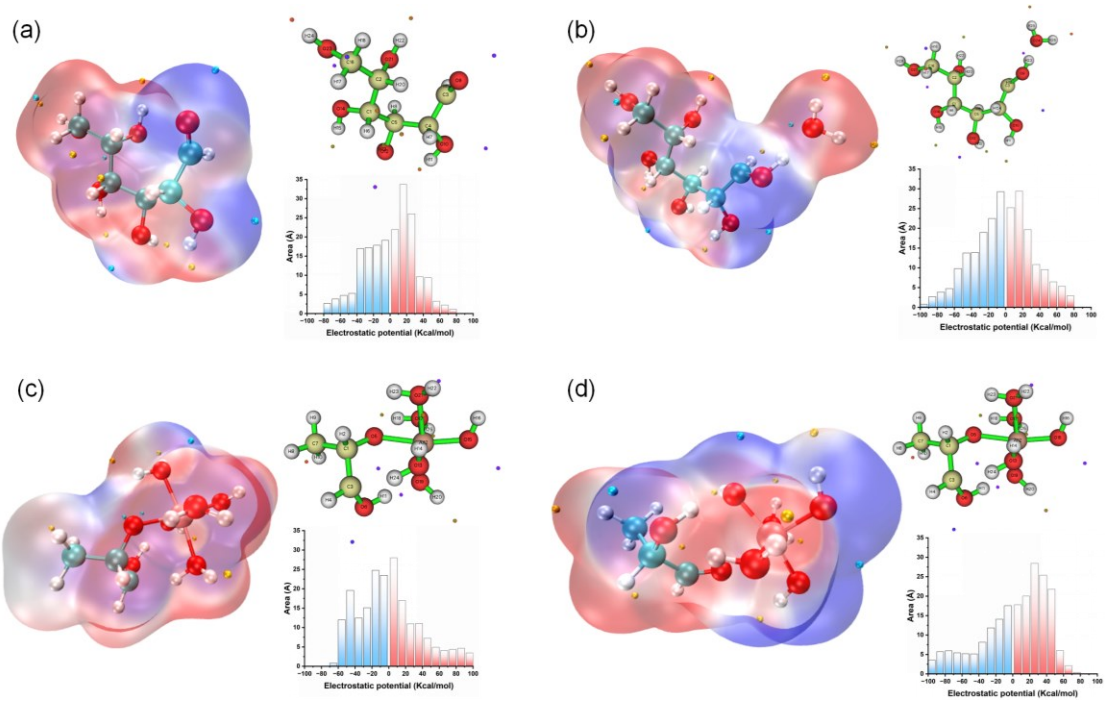

Fig. 10 Quantitative distribution of electrostatic potential of intermediates: (**a**) TS2, (**b**) TS3-2, (**c**) B2, and (**d**) B5.

Based on the DFT and wave function analysis, the results indicate the specific role of different active materials in the isomerization catalytic process. Among these active materials, MgO has a great effect on the ring-opening reaction to form acyclic glucose, while $Al(OH)_{3+}$ has a great effect on promoting acyclic glucose hydrogen transfer to form fructose. However, the excess Brønsted basic or Lewis acid

active materials will attack acyclic fructose to form acyclic glucose again through hydrogen transfer or proton transfer. Combined with the above results, tailoring suitable active materials in catalyst are important to achieve high glucose conversion rate and selectivity. Meanwhile, based on the quantum chemical calculation results and geometric optimization structure, we clarify the catalytic synergistic reaction mechanism of Brønsted basic (MgO) and Lewis acid ($Al(OH)^{3+}$) , as shown in **Fig. 11**. In **Fig. 11**, the pathway of MgO is divided into four steps: the ring opening of glucose to acyclic glucose (Reaction 1), the keto-enol tautomerism following the Lobry de Bruyn–van Ekenstein re-arrangement (Reaction 2), the formation of fructose from enediol intermediate (Reaction 3), and the cyclization of fructose (Reaction 4) . Different with Brønsted basic catalytic pathway, the Lewis acid catalytic pathway of $Al(OH)_3$ is divided into four steps: the ring opening of glucose to acyclic glucose (Reaction I), the $Al(OH)^{3+}$ sites interacting with carbonyl groups on acyclic glucose (Reaction II), the $Al(OH)^{3+}$ sites coordinating with acyclic glucose on the C1-O and C2-O positions and occurring intramolecular hydride shift (Reaction III), and the cyclization of fructose (Reaction IV). The synergistic effect is reflected in the fact that MgO will attack glucose with fast reaction rate to form acyclic glucose, while $Al(OH)^{3+}$ sites quickly coordinating with acyclic glucose on the C1-O and C2-O positions and occurring intramolecular hydride shift. This is will greatly improve the catalytic efficiency than either Brønsted basic or Lewis acid catalysis alone. The clarified catalytic mechanism will provide a theoretical basis for understanding the catalytic pathways of Lewis acid and Brønsted basic, thereby be beneficial to designing efficient catalyst for glucose isomerization.

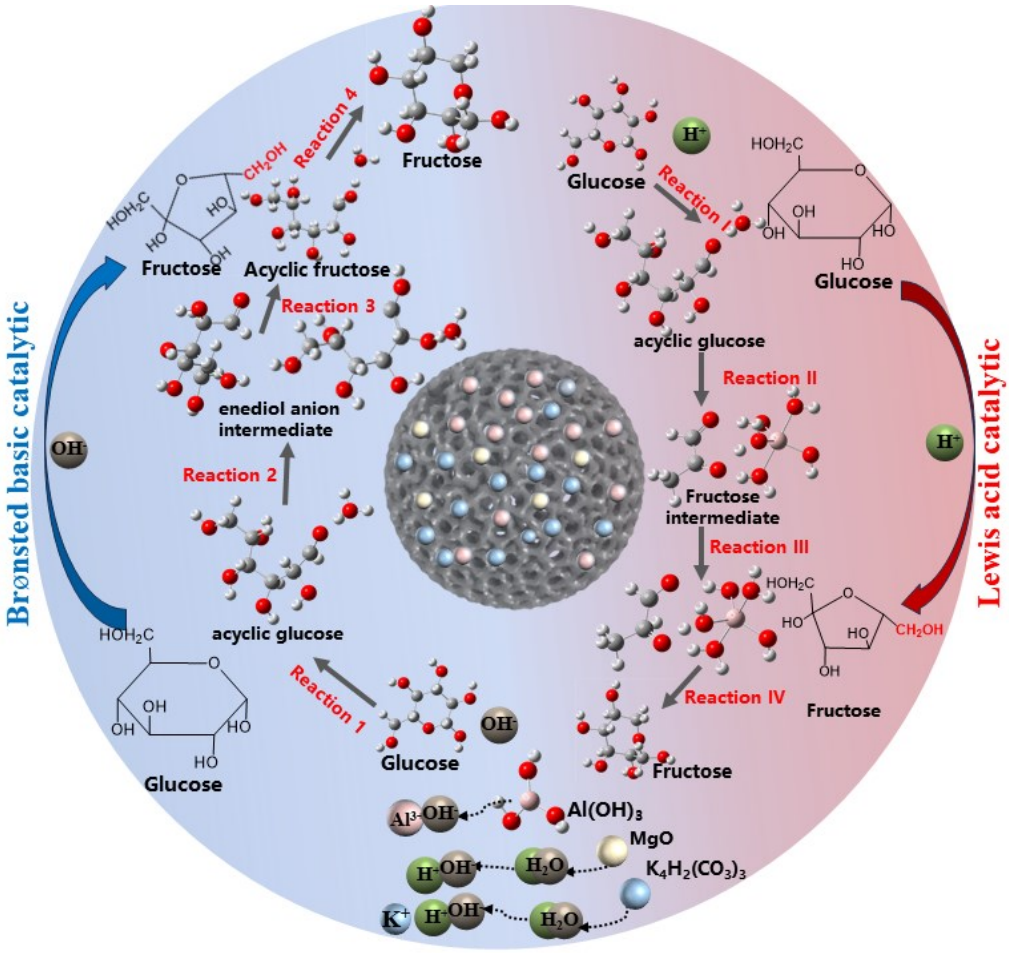

Fig. 11 Catalytic mechanism diagram of Mg-Al-K-C catalysts on glucose isomerization fructose.

4 Conclusion

A high-efficient glucose isomerization catalyst (Mg-Al-$KHCO_3$-C) was successfully synthesized and results in a 38.37% fructose yield, 87.82% fructose selectivity, and 44.12% glucose conversion rate at 100 °C for 30 min. The result of the catalyst illustrates that in Mg-Al-$KHCO_3$-C catalyst the highly O/Mg, O/Al ratio can provide more oxygen-unsaturated sites to induce H_2O ionization to form considerable OH^- ions, thus easily achieving the isomerization of glucose. Meanwhile, the main active sites (MgO, $Al(OH)_3$, and $K_4H_2(CO_3)_3$) in Mg-Al-$KHCO_3$-C can provide weakly acidic, basic sites, and avoid strongly acidic and basic sites to excess attack the glucose. Meanwhile, the results of DFT and wave function analysis point out that MgO has a great effect on the ring-opening reaction to form acyclic glucose, while

$Al(OH)^{3+}$ has a great effect on promoting acyclic glucose hydrogen transfer isomerize to form fructose. This work proves the feasibility of synthesizing multiple active sites high-efficient catalyst through easy hydrothermal carbonization and further calcination.

Supplementary information

The online version contains supplementary material available at

Funding This work was sponsored by the National Natural Science Foundation of China (grant no. 22268007); Natural Science Foundation of Guangxi Province, China (grant no. 2021GXNSFDA196006); Guangxi Science and Technology Major Pro-gram (Guike AA22117013); National Key Research and Development Program of China (grant no. 2021YFE0114400); Innovation Project of Guangxi Graduate Education (grant no. YCBZ2023020); and the Foundation of Guangxi Key Laboratory of Clean Pulp & Papermaking and Pollution Control, College of Light Industry and Food Engineering, Guangxi University (grant nos. 2021KF20). AJR efforts were supported University of Tennessee, Knoxvill.

Declarations

Conflict of interest The authors declare no competing interests.

Authorship contribution statement

Xiheng Kang: Conceptualization, Data curation, Investigation, Methodology, Project administration, DFT, Multiwfn, Supervision, Validation, Visualization, Writing-original draft, Writing-review & editing; Zi You: Methodology, Validation, Visualization; Yongheng Huang: Resources; Jian Peng: Software; Junhua Zhang: Methodology, Methodology; Arthur J.Ragauskas: Formal analysis, Funding acquisition, Writing-review & editing; Z. Zhang: Methodology, Methodology; Xueping Song: Methodology, Project administration, Supervision, Validation, Visualization, Writing-original draft, Writing-review & editing.

All authors have given approval to the final version of the manuscript.

References

[1] X. Kang, Y.Y. Wang, S. Wang, X. Song (2021) Xylan and xylose decomposition during hot water pre-extraction: A pH-regulated hydrolysis. Carbohydr Polym. 255: 117391. https://doi.org/10.1016/j.carbpol.2020.117391.

[2] B. Liu, L. Liu, B. Deng, C. Huang, J. Zhu, L. Liang, X. He, Y. Wei, C. Qin, C. Liang, S. Liu, S. Yao (2022) Application and prospect of organic acid pretreatment in lignocellulosic biomass separation: A review. Int J Biol Macromol https://doi.org/10.1016/j.ijbiomac.2022.09.270.

[3] X. Kang, Y.Y. Wang, S. Wang, X. Song (2021) Xylan and xylose decomposition during hot water pre-extraction: A pH-regulated hydrolysis. Carbohydr Polym 255: 117391. https://doi.org/10.1016/j.carbpol.2020.117391.

[4] L. Dai, J. Lu, F. Kong, K. Liu, H. Wei, C. Si (2019) Reversible photo-controlled release of bovine serum albumin by azobenzene-containing cellulose nanofibrils-based hydrogel. Adv Compos Hybrid Ma 2:(3) 462-470. https://doi.org/10.1007/s42114-019-00112-9.

[5] B. Hahn-Hägerdal, M. Galbe, M.F. Gorwa-Grauslund, G. Lidén, G. Zacchi (2006) Bio-ethanol – the fuel of tomorrow from the residues of today. Trends in Biotechnology 24:(12) 549-556. https://doi.org/10.1016/j.tibtech.2006.10.004.

[6] X. Yang, I.K.M. Yu, D.-W. Cho, S.S. Chen, D.C.W. Tsang, J. Shang, A.C.K. Yip, L. Wang, Y.S. Ok (2019) Tin-Functionalized Wood Biochar as a Sustainable Solid Catalyst for Glucose Isomerization in Biorefinery. ACS Sustain Chem Eng 7:(5) 4851-4860. https://doi.org/10.1021/acssuschemeng.8b05311.

[7] S. Saravanamurugan, M. Paniagua, J.A. Melero, A. Riisager (2013) Efficient isomerization of glucose to fructose over zeolites in consecutive reactions in alcohol and aqueous media. J Am Chem Soc 135:(14) 5246-9. https://doi.org/10.1021/ja400097f.

[8] M. Eqi, C. Shi, J. Xie, F. Kang, H. Qi, X. Tan, Z. Huang, J. Liu, J. Guo (2022) Synergetic effect of Ni-Au bimetal nanoparticles on urchin-like TiO2 for hydrogen and arabinose co-production by glucose photoreforming. Adv Compos Hybrid Ma 6:(1) https://doi.org/10.1007/s42114-022-00580-6.

[9] S. Zhao, G. Yue, X. Liu, S. Qin, B. Wang, P. Zhao, A.J. Ragauskas, M. Wu, X. Song (2023) Lignin-based carbon quantum dots with high fluorescence performance prepared by supercritical catalysis and solvothermal treatment for tumor-targeted labeling. Adv Compos Hybrid Ma 6:(2) https://doi.org/10.1007/s42114-023-00645-0.

[10] X. Liu, S. Zhao, X. Chen, X. Han, J. Zhang, M. Wu, X. Song, Z. Zhang (2024) The effect of lignin molecular weight on the formation and properties of carbon quantum dots. Green Chem https://doi.org/10.1039/d3gc04694j.
[11] H. Li, S. Yang, S. Saravanamurugan, A. Riisager (2017) Glucose Isomerization by Enzymes and Chemo-catalysts: Status and Current Advances. ACS Catalysis 7:(4) 3010-3029. https://doi.org/10.1021/acscatal.6b03625.
[12] X. Xiong, I.K.M. Yu, D.C.W. Tsang, L. Chen, Z. Su, C. Hu, G. Luo, S. Zhang, Y.S. Ok, J.H. Clark (2020) Study of glucose isomerisation to fructose over three heterogeneous carbon-based aluminium-impregnated catalysts. J Clean Prod 268: 122378. https://doi.org/10.1016/j.jclepro.2020.122378.
[13] I.K.M. Yu, A. Hanif, D.C.W. Tsang, J. Shang, Z. Su, H. Song, Y.S. Ok, C.S. Poon (2020) Tuneable functionalities in layered double hydroxide catalysts for thermochemical conversion of biomass-derived glucose to fructose. Chem Eng J 383: 122914. https://doi.org/10.1016/j.cej.2019.122914.
[14] J. Peng, X. Kang, S. Zhao, Y. Yin, P. Zhao, A.J. Ragauskas, C. Si, X. Song (2023) Regulating the properties of activated carbon for supercapacitors: impact of particle size and degree of aromatization of hydrochar. Adv Compos Hybrid Ma 6:(3) https://doi.org/10.1007/s42114-023-00682-9.
[15] X. Kang, J. Peng, A.J. Ragauskas, X. Ren, C. Si, S. Wang, X. Song (2022) Competitive effects of glucan's main hydrolysates on biochar formation: A combined experiment and density functional theory analysis. Bioresour Technol 359: 127427. https://doi.org/10.1016/j.biortech.2022.127427.
[16] J. Peng, X. Kang, S. Zhao, P. Zhao, A.J. Ragauskas, C. Si, T. Xu, X. Song (2023) Growth mechanism of glucose-based hydrochar under the effects of acid and temperature regulation. J Colloid Interface Sci 630:(Pt A) 654-665. https://doi.org/10.1016/j.jcis.2022.10.044.
[17] Y. Deng, T. Zhang, J. Clark, T. Aminabhavi, A. Kruse, D.C.W. Tsang, B.K. Sharma, F. Zhang, H. Ren (2020) Mechanisms and modelling of phosphorus solid–liquid transformation during the hydrothermal processing of swine manure. Green Chem. 22:(17) 5628-5638. https://doi.org/10.1039/d0gc01281e.
[18] M. Kim, S.-C. Jee, J.-S. Sung, A.A. Kadam (2020) Supermagnetic Sugarcane Bagasse Hydrochar for Enhanced Osteoconduction in Human Adipose Tissue-Derived Mesenchymal Stem Cells. Nanomaterials 10:(9) https://doi.org/10.3390/nano10091793.
[19] S. Zhang, K. Sheng, Y. Liang, J. Liu, S. E, X. Zhang (2020) Green synthesis of aluminum-hydrochar for the selective isomerization of glucose to fructose. Sci Total Environ. 727: 138743. https://doi.org/10.1016/j.scitotenv.2020.138743.
[20] I.K.M. Yu, X. Xiong, D.C.W. Tsang, L. Wang, A.J. Hunt, H. Song, J. Shang, Y.S. Ok, C.S. Poon (2019) Aluminium-biochar composites as sustainable heterogeneous catalysts for glucose isomerisation in a biorefinery. Green Chem. 21:(6) 1267-1281. https://doi.org/10.1039/c8gc02466a.
[21] S.Z. Kuichuan Sheng, Jianglong Liu, Shuang E, Caidi Jin, Zenghua Xu, Ximing Zhang (2019) Hydrothermal carbonization of cellulose and xylan into hydrochars and application on glucose isomerization. J Clean Prod. 237: 117831. https://doi.org/10.1016/j.jclepro.2019.117831.
[22] B. Li, M. Guo, X. Chen, Y. Miao (2022) Hydrothermally synthesized N and S co-doped mesoporous carbon microspheres from poplar powder for supercapacitors with enhanced performance. Adv Compos Hybrid Ma 5:(3) 2306-2316. https://doi.org/10.1007/s42114-021-00409-8.
[23] T. Xu, Y. Wang, K. Liu, Q. Zhao, Q. Liang, M. Zhang, C. Si (2023) Ultralight MXene/carbon nanotube composite aerogel for high-performance flexible supercapacitor. Adv Compos Hybrid Ma 6:(3) https://doi.org/10.1007/s42114-023-00675-8.

[24] Q. Fu, S. Yang, P. Ning, R. Miao, L. He, Q. Guan (2021) Construction of Dot-Matrix Cu0-Cu1Ni3 Alloy Nano-Dispersions on the Surface of Porous N-Autodoped Biochar for Selective Hydrogenation of Furfural. ChemCatChem. 13:(19) 4164-4181. https://doi.org/10.1002/cctc.202100882.
[25] J. Liu, M. Yang, C. Gong, S. Zhang, K. Sheng, X. Zhang (2021) Insights into the glucose isomerization mechanism of Al-hydrochar catalyst probed by Al-oxide species transformation. J Environ Chem Eng 9:(6) https://doi.org/10.1016/j.jece.2021.106721.
[26] J. Liu, X. Zhang, L. Yang, U.A. Danhassan, S. Zhang, M. Yang, K. Sheng, X. Zhang (2021) Glucose isomerization catalyzed by swollen cellulose derived aluminum-hydrochar. Sci Total Environ. 777: 146037. https://doi.org/10.1016/j.scitotenv.2021.146037.
[27] J.M. de Bruijn, A.P.G. Kieboom, H. van Bekkum (2010) Alkaline degradation of monosaccharides III. Influence of reaction parameters upon the final product composition. Recl. Trav. Chim. Pays-Bas 105:(6) 176-183. https://doi.org/10.1002/recl.19861050603.
[28] A.P.G.K. G. DE WIT, H.V. BEKKUM (1979) Enolisation and isomerisation of monosaccharides in queous, alkaline solution Carbohydr Res 74: 157-175. https://doi.org/10.1016/s0008-6215(00)84773-4
[29] C. Gong, N. Bryant, X. Meng, S. Bhagia, Y. Pu, D. Xin, C. Bender Koch, C. Felby, L.G. Thygesen, A. Ragauskas, S.T. Thomsen (2021) Double bonus: surfactant-assisted biomass pelleting benefits both the pelleting process and subsequent enzymatic saccharification of the pretreated pellets. Green Chem 23:(2) 1050-1061. https://doi.org/10.1039/d0gc03855e.
[30] W. Xie, F. Yao, H. Gu, A. Du, Q. Lei, N. Naik, Z. Guo (2022) Magnetoresistive and piezoresistive polyaniline nanoarrays in-situ polymerized surrounding magnetic graphene aerogel. Adv Compos Hybrid Ma 5:(2) 1003-1016. https://doi.org/10.1007/s42114-021-00413-y.
[31] C. Adamo, V. Barone (1999) Toward reliable density functional methods without adjustable parameters: The PBE0 model. J Chem Phys 110:(13) 6158-6170. https://doi.org/10.1063/1.478522.
[32] Y. Zhao, D.G. Truhlar (2008) The M06 suite of density functionals for main group thermochemistry, thermochemical kinetics, noncovalent interactions, excited states, and transition elements: two new functionals and systematic testing of four M06 functionals and 12 other functionals. Theor Chem Acc 119:(5-6) 525-525. https://doi.org/10.1007/s00214-007-0401-8.
[33] A. Schäfer, C. Huber, R. Ahlrichs (1994) Fully optimized contracted Gaussian basis sets of triple zeta valence quality for atoms Li to Kr. J Chem Phys 100:(8) 5829-5835. https://doi.org/10.1063/1.467146.
[34] A.V. Marenich, C.J. Cramer, D.G. Truhlar (2009) Universal Solvation Model Based on Solute Electron Density and on a Continuum Model of the Solvent Defined by the Bulk Dielectric Constant and Atomic Surface Tensions. J Phys Chem B 113:(18) 6378-6396. https://doi.org/doi.org/10.1021/jp810292n.
[35] X. Kang, Z. You, J. Peng, A.J. Ragauskas, J. Pang, P. Zhao, Y. Yin, X. Song (2023) Synthesis of Mg–K-biochar bimetallic catalyst and its evaluation of glucose isomerization. Biochar 5:(1) https://doi.org/10.1007/s42773-023-00250-w.
[36] S. Wang, D. Guo, R. Kang, J. Feng, H. Pan (2023) Fabrication of lignin-derived mesoporous carbon/magnesium oxide composites for microwave-assisted isomerization of glucose in water. Int J Biol Macromol 232: 123341. https://doi.org/10.1016/j.ijbiomac.2023.123341.
[37] X. Chai, H. He, H. Fan, X. Kang, X. Song (2019) A hydrothermal-carbonization process for simultaneously production of sugars, graphene quantum dots, and porous carbon from sugarcane bagasse. Bioresour Technol. 282: 142-147. https://doi.org/10.1016/j.biortech.2019.02.126.

[38] S. Yu, E. Kim, S. Park, I.K. Song, J.C. Jung (2012) Isomerization of glucose into fructose over Mg–Al hydrotalcite catalysts. Catalysis Communications 29: 63-67. https://doi.org/10.1016/j.catcom.2012.09.015.
[39] S. Zhang, J. Wang, S. Zhu, X. Liu, Y. Xiong, H. Zhang (2020) Effects of MgCl2 and Mg(NO3)2 loading on catalytic pyrolysis of sawdust for bio-oil and MgO-impregnated biochar production. J Anal Appl Pyrol. 152: https://doi.org/10.1016/j.jaap.2020.104962.
[40] F. Shen, J. Fu, X. Zhang, X. Qi (2019) Crab Shell-Derived Lotus Rootlike Porous Carbon for High Efficiency Isomerization of Glucose to Fructose under Mild Conditions. ACS Sustain Chem Eng. 7:(4) 4466-4472. https://doi.org/10.1021/acssuschemeng.8b06512.
[41] P. Suttibut, K. Suriye, S. Kunjara Na Ayudhya, P. Praserthdam, J. Panpranot (2015) Effect of N2 pretreatment on the basicity, structural change, and isomerization activity of MgO and MgO/Mg(OH)2 catalysts. Asia-Pac J Chem Eng 10:(2) 248-258. https://doi.org/10.1002/apj.1869.
[42] S.S. Chen, Y. Cao, D.C.W. Tsang, J.-P. Tessonnier, J. Shang, D. Hou, Z. Shen, S. Zhang, Y.S. Ok, K.C.W. Wu (2020) Effective Dispersion of MgO Nanostructure on Biochar Support as a Basic Catalyst for Glucose Isomerization. ACS Sustain Chem Eng. 8:(18) 6990-7001. https://doi.org/10.1021/acssuschemeng.0c00278.
[43] V. Mutreja, S. Singh, A. Ali (2011) Biodiesel from mutton fat using KOH impregnated MgO as heterogeneous catalysts. Renew Energ. 36:(8) 2253-2258. https://doi.org/10.1016/j.renene.2011.01.019.
[44] L. Yang, E. Shuang, J. Liu, K. Sheng, X. Zhang (2022) Endogenous calcium enriched hydrochar catalyst derived from water hyacinth for glucose isomerization. Sci Total Environ. 807:(Pt 2) 150660. https://doi.org/10.1016/j.scitotenv.2021.150660.
[45] J.M. Carraher, C.N. Fleitman, J.-P. Tessonnier (2015) Kinetic and Mechanistic Study of Glucose Isomerization Using Homogeneous Organic Brønsted Base Catalysts in Water. ACS Catal. 5:(6) 3162-3173. https://doi.org/10.1021/acscatal.5b00316.
[46] H. Liu, H. Wang, X. Lu, V. Murugadoss, M. Huang, H. Yang, F. Wan, D.-G. Yu, Z. Guo (2022) Electrospun structural nanohybrids combining three composites for fast helicide delivery. Adv Compos Hybrid Ma 5:(2) 1017-1029. https://doi.org/10.1007/s42114-022-00478-3.
[47] G. Yin, L. Tao, X. Chen, N.S. Bolan, B. Sarkar, Q. Lin, H. Wang (2021) Quantitative analysis on the mechanism of Cd(2+) removal by MgCl(2)-modified biochar in aqueous solutions. J Hazard Mater 420: 126487. https://doi.org/10.1016/j.jhazmat.2021.126487.
[48] A.M. Norton, H. Nguyen, N.L. Xiao, D.G. Vlachos (2018) Direct speciation methods to quantify catalytically active species of AlCl(3) in glucose isomerization. RSC Adv 8:(31) 17101-17109. https://doi.org/10.1039/c8ra03088j.
[49] I.K.M. Yu, D.C.W. Tsang, A.C.K. Yip, S.S. Chen, Y.S. Ok, C.S. Poon (2016) Valorization of food waste into hydroxymethylfurfural: Dual role of metal ions in successive conversion steps. Bioresour Technol 219: 338-347. https://doi.org/10.1016/j.biortech.2016.08.002.
[50] T. Lu, Q. Chen (2021) Interaction Region Indicator: A Simple Real Space Function Clearly Revealing Both Chemical Bonds and Weak Interactions**. Chemistry–Methods 1:(5) 231-239. https://doi.org/10.1002/cmtd.202100007.
[51] T. Lu, F. Chen (2012) Multiwfn: a multifunctional wavefunction analyzer. J Comput Chem 33:(5) 580-92. https://doi.org/10.1002/jcc.22885.
[52] T. Lu, F. Chen (2012) Quantitative analysis of molecular surface based on improved Marching Tetrahedra algorithm. J Mol Graph Model 38: 314-23. https://doi.org/10.1016/j.jmgm.2012.07.004.